2009

Plasmonic Bragg reflector and its application on optical switching

Yu Liu
Iowa State University

Plasmonic Bragg reflector and its application on optical switching

by

Yu Liu

A thesis submitted to the graduate faculty

in partial fulfillment of the requirements for the degree of

MASTER OF SCIENCE

Major: Electrical Engineering

Program of Study Committee:
Jaeyoun Kim, Major Professor
Jiming Song
Zhao Zhang

Iowa State University

Ames, Iowa

2009

TABLE OF CONTENTS

LIST OF FIGURES

ACKNOWLEDGEMENTS

Thanks to my Major Professor, Jaeyoun Kim, for his patient guidance and support throughout this entire project. Thanks to my committee members for their efforts and support to this work: Dr. Jiming Song and Dr. Zhao Zhang.

Thanks to my group members: Jiwon Lee, Yifen Liu and Yafang Tang, for all their help in my graduate life.

Also, thanks to those who helped me with my research and the writing of this thesis.

Special thanks to my family for all the love over these years of school.

ABSTRACT

In nowadays intergrated circuit design, the diffraction limit has restricted the downscaling of the conventional electronic components. Surface Plasmon Polaritons (SPPs) are quantized charge density oscillations that occur at the interface between metal and dielectric materials when photons couple to the free electron gas of the metal. The extraordinary properties of SPPs can be utilized for sub-diffraction limit wave guiding and localized field enhancement. The resulting photonic components overcome the physics limitations of their electronic counterparts and offer a promising vista of the next generation all-optic circuits.

Among all possible plasmonic-based configurations, those focus light into the dielectric core in a metal-insulator-metal(MIM) structure allow the manipulation and transmission of light at the nanoscale. Based on MIM structures, plasmonic Bragg reflectors reveal similar properties as the distributed Bragg reflectors. Therefore, plasmonic Bragg reflectors may also be used for effective optical switching, when the similar design for distributed Bragg reflectors is applied.

In this thesis, the sawtooth plasmonic Bragg reflector and the nonlinear $\lambda/4$-shifted plasmonic Bragg reflector is proposed and studied. The obtained simulation results grant a better understanding of the characteristics of plasmonic Bragg reflectors and demonstrate their outstanding performance on optical switching.

CHAPTER 1. INTRODUCTION

1.1 Background

Electronic circuits provide us with the ability to control the transport and storage of electrons thus offer the capability of digital signal transportation. However, further improvement of the performance of electronic circuits nowadays is becoming rather limited as the dimensions of today's state-of-the art microprocessors are on the order of 50 nm and are trying to further goes down. The performance of a high-speed electronic chip is highly dependent on interconnects, which connect different macro cells within an integrated chip. In order to scale down the electronic circuits, the scaling of copper wire interconnect is inevitable. While the transistor performance increases with exponentially increasing transistor count, the scaling of metallic wires turned out to be problematic. First of all, the impedance increases for scaled metallic wires which cannot provide efficient connections for the data transferring between macro electronic cells, which might be a few centimeters away from each other; secondly, the delay due to interconnects increases and greatly limits the speed of electronic circuits [1]. Optical interconnects such as fibers can carry digital data with a capacity much bigger than that of electronic interconnects, making them a possible solution for the current limitations in electronic circuits. However, traditional optical communicating components are bulk with a core size of tens of even hundreds of microns not mentioning the much bigger cladding size compared to electronic components in nanoscales. Even though optical interconnects offer prominent data transferring capabilities that is not limited by the resistance, capacitance, the electron scattering issues [2] of metallic wires, it is very difficult to combine optical and electronic components on the same circuit because the generation, transportation and detection of electrons and photons are all quite different.

There are approaches to integrate microelectronic and microphotonics into the same chip based on silicon [2, 3, 4]. But some of the approaches are still based on the transduction of photons to electrons and the electronic processing components and cannot fully incorporate optical components and explore their potential in ultra fast optical circuits. Unlike electronic integration where silicon is the dominant material, systematic optical integrated circuits have been fabricated from a variety of material systems, including silica on silicon, silicon on insulator, lithium niobate crystals modified with the titanium diffusion [5], as well as various polymers and semiconductor materials [6, 7]. Besides the availability of various materials, optical signal processing offers higher speed, and since optical circuits transfer signals at light wave frequencies, they are less possibly to be affected by electromagnetic interference [8]. This is why all optical circuits are gaining increasing academic and industrial interest.

The concept of "integrated optics" emerged in the late 1960s, in which the wires and radio links in conventional electrical integrated circuits are replaced by light-guiding optical fibers [9]. For the modern concept of integration, optical fiber is somehow too bulky and in the year of 1977, P. K. Tien stated that [10, abstract] "Research in integrated optics has two goals: one is to apply thin film technology to the formation of optical devices and circuits, the other is the integration of a large number of optical devices on a small substrate, so forming an optical circuit reminiscent of the integrated circuit in microelectronis" and miniaturized optical components such as lasers, detectors, lens, couplers, modulators, switches and et. al. have been studied and constructed since then [10].

Recently proposed integrated optical components include photodetector [11, 12], modulators [13, 14], integrated lasers based on silicon-on-insulator (SOI) rib waveguide [15] and based on hybrid AlGaInAs-silicon platform [12]. Optical switch, which is a key component that limits the speed of integrated circuits, has also gained great interest.

Using photonic crystal is a common approach for optical switching since photonic crystal makes it possible to control the local optical response of the photonic crystal to an optical signal with a second optical control signal [16]. Kiyoshi Asakawa, Yoshimasa Sugimoto et. al. have demonstrated ultra-fast (∼ps) and ultra-low energy (∼100 fJ) switching using GaAs-based two-

dimensional photonic crystal (2DPC) slab waveguides (WGs) with a chip of 600μm×300μm in size [17]. Akihiko Shinya, Takasumi Tanabe et. al. have demonstrated a fast switching operation of about 100 ps with a very low energy of a few tens of femtojoules based on coupled resonator-waveguide systems in two-dimensional Si-based photonic crystals [18]. However, all the optical switches based on photonic crystal are active devices which might causes more circuitry complexity due to a second control signal. Another problem with photonic crystals is that they usually involves complicate fabrication, even the simple one dimensional photonic crystal requires depositing many layers.

Other approaches include using multimode interference coupler and the switching employs the thermo-optic effect of polymers. The 22 mW switching power is much higher than those using photonic crystal. Yet, external heaters are required for this switch [19]. Recently, Stephan T. Dubas and Vimolvan Pimpan demonstrated optical color switching using silver nanocomposite thin films, the color switch occurs in less than a sec. But they used ethanol and water exposure as the switching operation, and the optical transmittance change is due to the shift in the silver plasmonic absorbance band due to the changes in the dielectric constant of the surrounding medium. This makes their structure more suitable for sensing purpose, but not for integrated optic circuits [20].

While most of the examples listed here are based on conventional optical materials or semiconductors, future scaling down of these integrated components will be difficult due to the diffraction limit of light which means when the dimensions of an optical component become close to the wavelength of light, the propagation of light is obstructed by optical diffraction and the diffraction is the main limitation of the sizes of optical components and optical integrated circuits. For the achievement of integrated photonic components with nanoscale feature sizes, surface plasmon polaritions (SPPs) has been the main approach to circumvent this limitation in miniaturization of optical components.

SPPs are surface waves along metal-dielectric interfaces and they hold high potential for nanoscale optical circuits because both the waveguiding structure and the SPP modes can be achieved in nanoscale. Beside the potent compact optical components with SPP waves,

plasmonic circuits offer the potential to carry optical signals and electric currents through the same component [1]. Metallic wires have been used for electronic signals as long as the invention of integrated electronic circuits, while the metal-dielectric interfaces also support SPPs with optical waves/signals. As a result, the SPP also holds the ability to combine both the advantages of photonics and electronics on the same chip. Due to its surface wave nature and subwavelength confinement, SPP has been used for Surface Enhanced Raman Spectroscopy (SERS) [21] and other spectroscopies [22]. SPPs have also gain much investigation in chemical and biomedical surface sensing [23].

Typical metals that support SPPs are silver and gold, but metals such as copper, titanium or chromium are also possible for SPP excitation, yet with much lower efficiency. Generally speaking, materials with dielectric constants that have a negative real part and a small positive imaginary part are capable of supporting a SPR. This is why artificially engineered nanostructured metamaterials that possess a negative refractive index at optical wavelengths have been intensively studied [24] and SPPs have been generated at the interface between metamaterials and dielectric materials [25]. The feasibility of plasmonic integrated optical components has also been intensively studied [26].

There are generally two types of plasmonic structures used for SPPs guiding, using thin ($\sim$50 nm) metal films sandwiched between two dielectric layers and semi-infinite metal layers together with finite dielectric thin layers, these two types can be simply viewed as insulator-metal-insulator (IMI) structures and metal-insulator-metal (MIM) structures and they are shown in Fig. 1.1 respectively [27].

Recently, many strutures based on the MIM guiding has been studied, including some plasmonic Bragg reflectors [28, 29]. They show very similar pass/stop band characteristics as the tradictional Bragg reflectors. Meanwhile, the same transmission peak exists inside the stop band when a quarter wavelength defect is introduced at the center of the structure. This abrupt change of the transmission has been exploited to design switching components, in both the electronic circuits [30] and the optic circuits [31, 32]. However, most of the latter kind of structures are based on photonic microcavity scheme and therefore require special materials

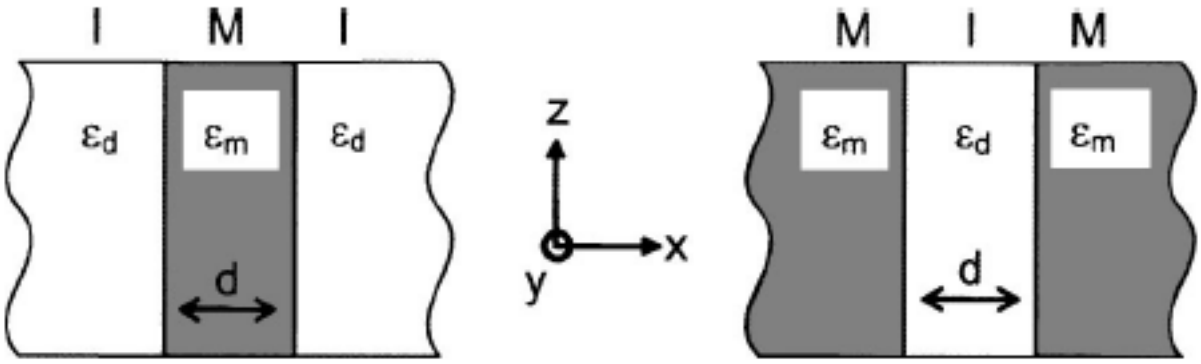

Figure 1.1 Insulator-metal-insulator (IMI) (left) and metal-insulator-metal (MIM) (right) geometries supporting SPP modes [27].

and fabrications to achieve enough confinement inside the cavity.

Therefore, in this thesis, optical switch based on nonlinear $\lambda/4$-shifted plasmonic Bragg reflector structure is proposed and investigated. It shows great performance on optical switching. Meanwhile, a sawtooth plasmonic Bragg reflector structure is also studied as it can reduce the extra energy loss caused by MIM mode mismatching.

1.2 Organization of this thesis

Chapter 2 investigates main theoretical backgrounds involving SPPs, MIM, and plasmonic Bragg reflectors. It also analyzes the design of nonlinear $\lambda/4$-shifted plasmonic Bragg reflectors for the purpose of optic switching.

Chapter 3 focuses on the specification of the proposed structures: the sawtooth plasmonic Bragg reflector and the nonlinear $\lambda/4$-shifted plasmonic Bragg reflector. It also introduces the simulation methodologies including FEM and FDTD, and the software used in this project: COMSOL and MEEP.

Chapter 4 concentrates on the simulation results and corresponding analyses.

Chapter 5 presents a summary of this thesis.

CHAPTER 2. THEORETICAL BACKGROUND

2.1 Drude Model

As first proposed by Paul Drude in 1900 [33, 34], the Drude model has gain wide use in explaining the transport properties of electrons in materials [35]. The Drude model, which is an application of kinetic theory, examines the electrical conduction based on several assumptions as listed below [35, 36]:

1. Interactions between electrons collisions are neglected, which means the microscopic behavior of electrons is treated classically and free electron approximation is used. In other words, electrons are constantly bouncing and re-bouncing off heavier, relatively immobile positive ions.

2. The collisions between electrons and ions and between different electrons happened instantaneous.

3. The relaxation time of electrons is τ, which means collisions occur on average every τ seconds. And the probability of collision is $1/\tau$.

4. Local thermal equilibrium is also assumed. Electron velocity after collision is temperature dependent.

Though the Drude model works for insulators and semiconductors too, it has been applied mostly for modeling of metals. This is because the thermal velocity of electrons should be sufficiently high to satisfy the modal assumptions above. While for metals, the Drude model provides a very good explanation of DC and AC conductivity. The frequency-dependent AC conductivity directly affects the dielectric constant and the plasma frequency of metals. It

also well explains the Hall effect, the Wiedemann-Franz law, and thermal conductivity due to electrons in metals [35]. Even though the Drude model greatly overestimates the electronic heat capacities of metals [35], it does not affect research and applications involving only the dielectric constant of metals as in this thesis.

In Drude model, The dielectric constant of a metal is given by [36]:

$$\epsilon(\omega) = \epsilon_\infty - \frac{\omega_p^2}{\omega(\omega + i\Gamma)} \tag{2.1}$$

where ω_p is the plasma frequency, and Γ is the damping coefficient.

It has been known that this free-electron Drude model was not adequate in the visible and the near-IR wavelength range [37], but for wavelengths longer than that the Drude model can provide good estimation of the dielectric constants of metals. The wavelength range used in this thesis is 800 nm$\sim$2600 nm, so the Drude model can be very accurate for our study.

2.2 Surface plasmon polaritons

SPPs result from the resonant interaction between electron-charged oscillations near the surface of the metal and the electromagnetic field of the light inside a dielectric medium. So, it is sometimes called surface plasmon resonance (SPR), which is the resonance excitation of SPP modes. SPPs are trapped near a metal-dielectric as they interact with the plasma of electrons near the surface of the metal and the electromagnetic waves near the surface of the dielectric layer. As a result, SPP modes are generated as surface waves propagating along the dielectric-metal interface and having evanescent field inside both the dielectric and the metal layers. The electron/optical wave resonance and the resulting SPP mode are shown in Fig. 2.1(a) and Fig. 2.1(b) respectively.

Generally speaking, the SPPs will propagate in both x- and y- directions along the dielectric-metal interface [22]. The propagating distance of SPPs can be on the order of tens to hundreds of microns [22, 23]. And penetration depths along the z-direction, taken as the evanescent decay lengths with $1/e$ power, are on the order of 200$\sim$400nm and $\sim$20nm inside the dielectric layer and metal layer, respectively [23].

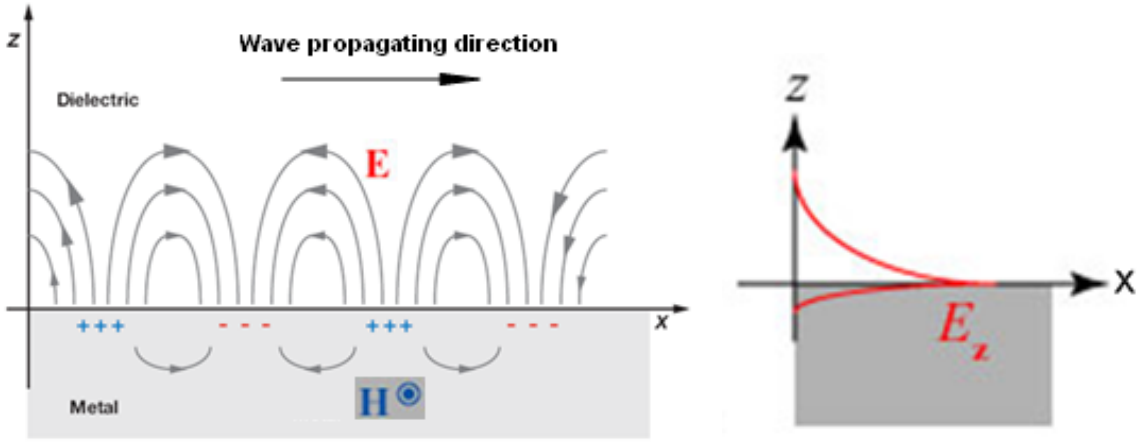

(a) the electric field inside the dielectric layer and the free charge oscillations inside the metal layer [22]

(b) the SPP wave propagating along the dielectric/metal interface [38]

Figure 2.1 Surface plasmon polaritons at a dielectric and metal interface.

2.2.1 Excitation of SPPs

P-polarized waves (TM waves, the polarization is parallel to the plane of incidence) has been used for generating SPPs and s-polarized waves (TE waves, the polarization is perpendicular to the plane of incidence) light cannot excite SPPs. Besides, in order to get surface plasmons polaritons, the resonant excitation conditions require the momentum of the incoming photons being matched to that of the plasmon, i.e. the phase velocities of the optical wave inside the dielectric layer and the the plasmon inside the metal layer must be strictly matched. This momentum matching between the optical wave and the plasmon can be achieved using several different schemes. For thin metal film based SPPs, this momentum matching is obtained by passing the light through a glass prism to increase its phase velocity before it hits the metal-dielectric interface or using a grating to modify the phase velocity of the light. These two methods are shown in Fig. 2.2 [23].

These configurations have been widely used for SPR applications so far, yet the resonant excitation can be achieved under certain wavelengths and definite angles, which means stringent optical alignment is required for the SPR generation and also the prism block in Fig. 2.2(a) are quite bulky and greatly sacrifice the size advantage of the sub-wavelength waveguiding of

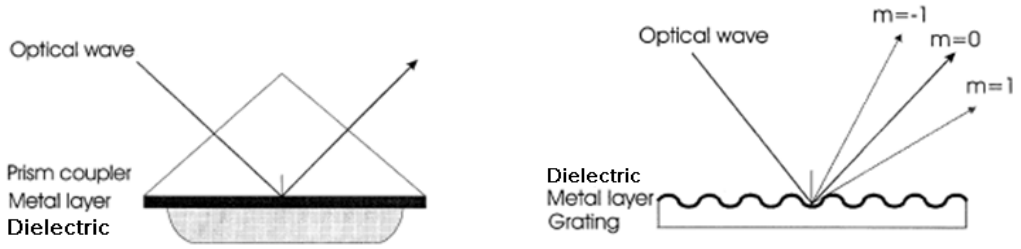

(a) prism coupler-based SPR system (ATR method)

(b) grating coupler-based SPR system

Figure 2.2 Excitation methods of SPPs [23, revised].

SPPs.

SPPs have exponentially decaying fields inside both the metal and dielectric layers as mentioned before. The decay lengths are less than 1μm, which are orders of magnitude smaller than the free space wavelength of the excitation light. This feature of SPPs provides the possibility of localization and the guiding of light in subwavelength structures, thus can be used in miniaturized optical circuits with subwavelength optical confinement. However, for miniaturization of plasmonic components, the miniaturization of SPP supporting structures are highly demanded for the future integrated optic circuits. SPPs excitation supported by thin metal films based on the evanescent tails of waveguide modes have also been proposed but had not got good performance yet [23].

Other nominates for compact SPR excitation scheme include using a thin dielectric layer sandwiching between two bulk metal layers which is called metal-insulator-metal (MIM) structure, or a thin metal film sandwiching between two bulk dielectric layer which is called insulator-metal-insulator (IMI) structure. MIM is more suitable for integrated purposes because they act as plasmonic waveguides for which the SPP modes can be directly excited from a perpendicular incidence of the free space light to the end face of MIM or IMI structure without the need of momentum matching. MIM structure is more preferable over IMI since it has stronger mode confinement for optical application and our design is based on this MIM scheme which will be discussed later in more details.

2.2.2 Equations

After success excitation, SPPs along a metal-dielectric interface obey the following dispersion relation [39]:

$$K(\omega) = \frac{\omega}{c}\sqrt{\frac{\epsilon_1\epsilon_2\mu_1\mu_2}{\epsilon_1\mu_1 + \epsilon_2\mu_2}} \tag{2.2}$$

where $K(\omega)$ is the wavelength dependent wavenumber of the SPPs and ω is the free space wavenumber, ϵ_1 and ϵ_2 stands for the dielectric constant of the metal layer and dielectric layer respectively, μ_1 and μ_2 stands for the magnetic permeability of the metal layer and dielectric layer.

The materials used in SPP applications are usually non-magnetic materials with $\mu = 1$, and $K_{sp}(\omega)$ is complex due to the complex and wavelength dependent dielectric constant of metal $\epsilon_1(\omega) = \epsilon_1'(\omega) + j\epsilon_1''(\omega)$. Then $K_{sp}(\omega)$ can be written as [40]:

$$K_{sp}(\omega) = K_{sp}'(\omega) + jK_{sp}''(\omega) \tag{2.3}$$

and the real part and imaginary part of $K_{sp}(\omega)$ are [40]:

$$\begin{aligned} K_{sp}'(\omega) &= \frac{\omega}{c}\sqrt{\frac{\epsilon_1'(\omega)\epsilon_2(\omega)}{\epsilon_1'(\omega) + \epsilon_2(\omega)}} \\ K_{sp}''(\omega) &= \frac{\omega}{c}\left(\frac{\epsilon_1'(\omega)\epsilon_2(\omega)}{\epsilon_1'(\omega) + \epsilon_2(\omega)}\right)^{\frac{3}{2}}\frac{\epsilon_1''(\omega)}{2\epsilon_1'(\omega)^2} \end{aligned} \tag{2.4}$$

2.3 Metal-insulator-metal structure

Both insulator-metal-insulator (IMI) and metal-insulator-metal (MIM) structures can be employed for SPP excitation and guiding of the SPP modes. IMI structures have less loss, and thus longer propagation length, but they suffer from poor confinement of light. MIM-type waveguides have been shown to be much more efficient for subwavelength confinement though

MIM SPP modes have shorter yet still acceptable propagation length [27]. The center layer thickness for IMI and MIM is usually between 30 nm to 100 nm. Due to the thin insulator thickness, the interaction between SPPs supported by the two metal-dielectric surfaces are strong and the dispersion curve of a single interface splits into high and low-energy modes. However, due to structural symmetry, only the low-energy mode is excited [41]. For comparison of mode characteristics of SPPs supported by MIM and IMI structures, the propagation length and the confinement factor for the low-energy SPP modes are shown in Fig. 2.3. And only this low-energy SPP mode is considered in this thesis.

Due to the better light confinement offered by MIM structure, MIM based structure in integrated circuit can be more compact and be less affected by optic components nearby, making it more suitable for integrated purposes. The dispersion relation of an MIM structure with finite metal layer thickness of d and two semi-infinite metal layers is governed by the following equation [42]:

$$tanh\left(\frac{1}{2}\alpha_1 d\right) = -\frac{\epsilon_1 \alpha_2}{\epsilon_2 \alpha_1} \tag{2.5}$$

where ϵ_1 and ϵ_1 are the dielectric constants of the insulator and the metal, respectively. d is the width of the inner insulator. α_1 and α_2 are the transverse propagation constants in the insulator and the metal, respectively, which are related to the effective index of refraction n_{eff} as [42]:

$$\alpha_i = k_0\sqrt{n_{eff}^2 - \epsilon_i}, (i = 1, 2) \tag{2.6}$$

From Eqn. 2.5 and 2.6, the effective index of MIM SPP mode is very dependent on the width of the insulator and the permittivities of both the metal layers and the insulator. For higher SPR efficiency, Ag and Au are commonly used as the metal layer. Thus the effective index can be controlled by modifying the insulator thickness and refractive index. The refractive index of Ag and Au is very wavelength-dependent, thus the dispersion of SPP modes is very important. For better understanding, the dispersion curves for this SPP mode are shown in

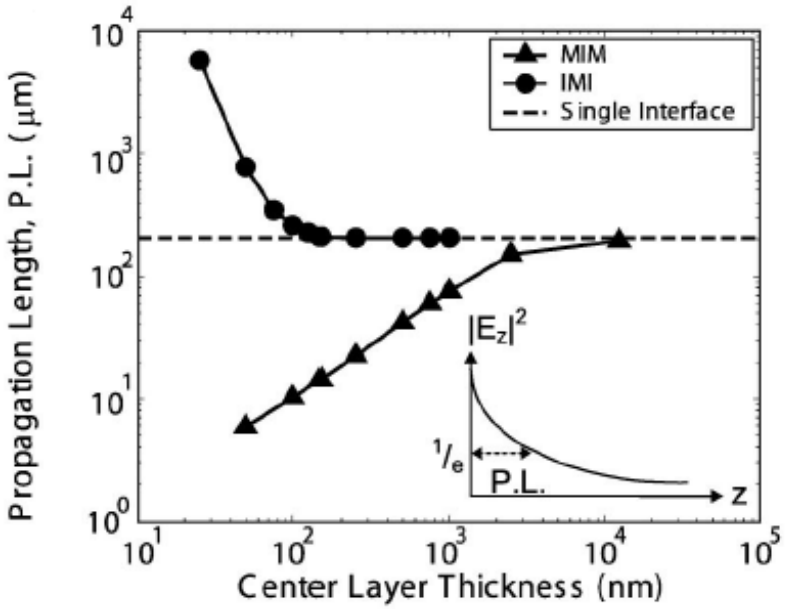

(a) propagation length as a function of decreasing center layer thickness for MIM and IMI SPP modes.

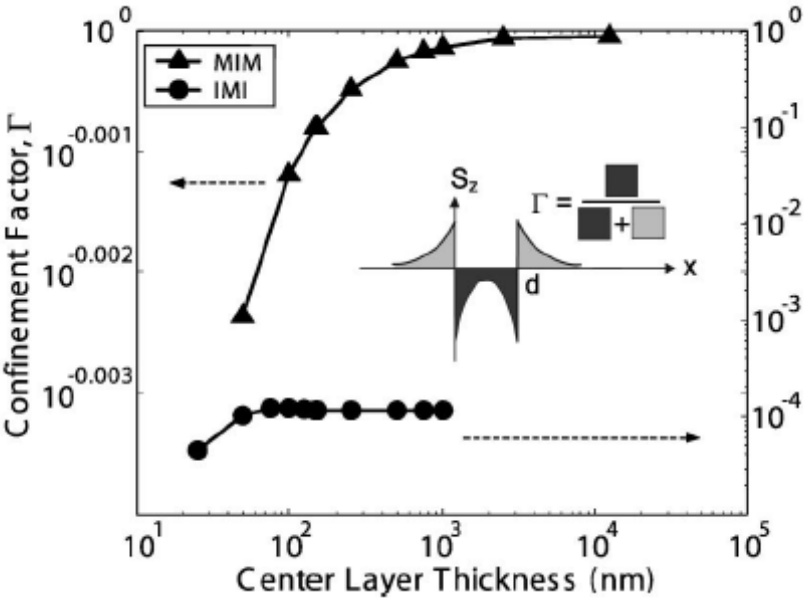

(b) confinement factor as a function of decreasing center layer thickness for MIM and IMI SPP modes.

Figure 2.3 The propagation length and the confinement factor for the low-energy SPP modes [27]. Au and air are used as the metal and the insulator respectively. The wavelength is set at 1550 nm for the calculation.

Fig. 2.4 for different insulator thickness [41], while Au is used for the metal layers and a SiO_2 layer is used as the insulator.

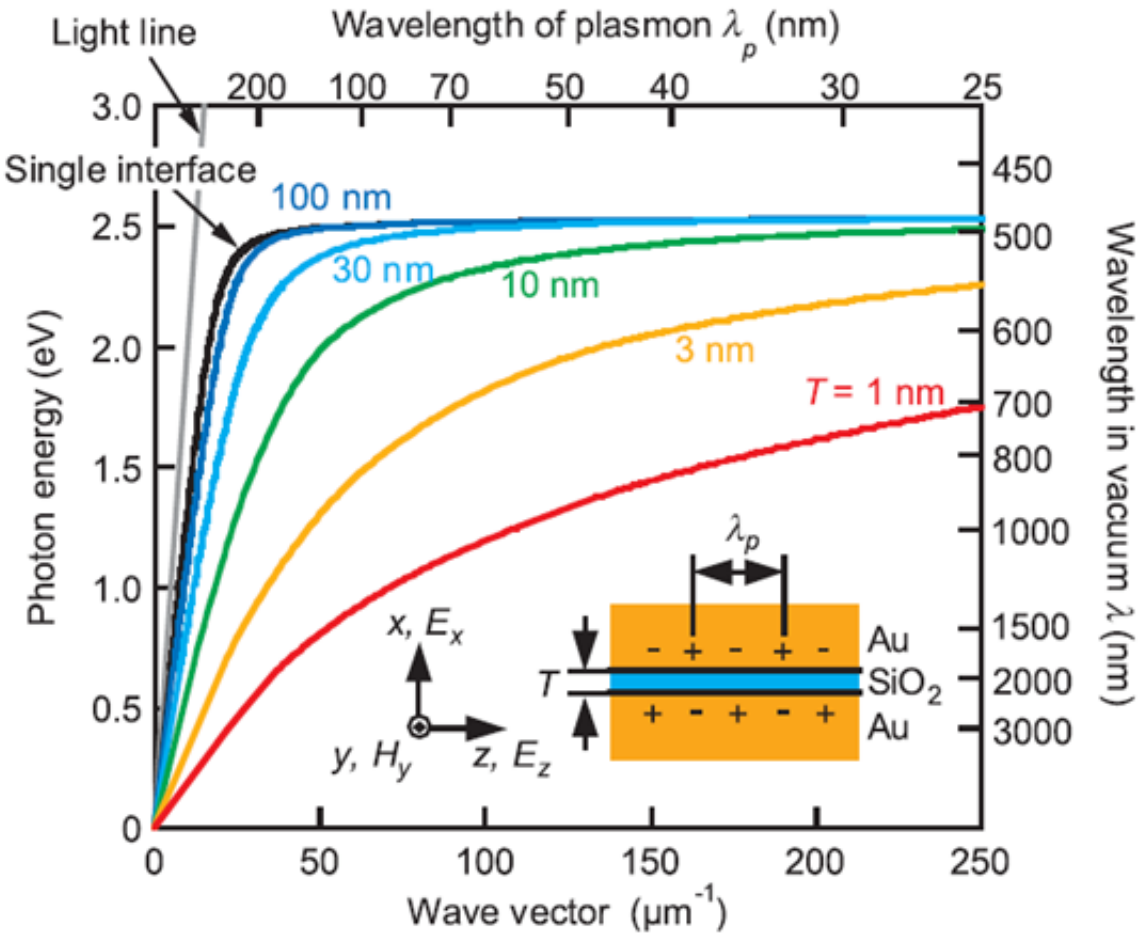

Figure 2.4 Dispersion relations of SPP modes propagating in z-direction supported by a MIM structure. The geometry and the field components are shown in the inset. For comparison, the dispersion for SPPs supported by a single Au/SiO_2 interface is added as the black solid curve [41].

From Fig. 2.4, we can clearly confirm that the effective indices of SPP modes supported by MIM structures are strongly dependent on the thickness of the insulator slit. This offers us a wide range for engineering the refractive index of SPPs for desired applications.

2.4 Bragg reflector

A Bragg reflector (also called distributed Bragg reflector, Bragg mirror) is a periodic structure consisting of multiple thin-film layers with alternating high index and low index materials. For efficient reflection under normal incident of light, the most frequently used design is called $\lambda/4$-shifted Bragg reflector, which is also called quarter-wave Bragg reflector [43]. For a $\lambda/4$-shifted Bragg reflector, the structure is designed so that the following Bragg condition is met:

$$\lambda_B = 4 \cdot d_H \cdot n_H = 4 \cdot d_L \cdot n_L \tag{2.7}$$

where λ_B is called the Bragg wavelength, d_H and d_L are the thicknesses of high and low index layers respectively, n_H and n_L are the refractive indices of high and low index layers respectively.

The Bragg condition is satisfied at the Bragg wavelength λ_B, while the optical path length difference between reflections from subsequent interfaces is half the wavelength [44]. As a result, the reflected lights from different interfaces are all in phase and the constructive interface leads to strong reflection. This strong reflection can be achieved around the λ_B for a certain wavelength range which is called the bandgap, which is also called photonic stopband in which light is "forbidde" to propagate in the structure [43]. So a common reflection spectrum from a Bragg reflector is shown in Fig. 2.5, while the bandgap of the Bragg reflection is given by [43]:

$$\Delta\lambda = \frac{4\lambda_B}{\pi} arcsin\left(\frac{n_H - n_L}{n_H + n_L}\right) \tag{2.8}$$

The high reflection from Bragg reflection has gain wide application in distributed Bragg reflector (DBR) lasers [45, 46]. However, by introducing a defect into the periodicity of the Bragg reflector, a defect mode will be generated inside the bandgap [47], as shown in Fig. 2.6; around which the reflectivity will be dramatically reduced and a large portion of the incident light will pass through the Bragg reflector. The defect can be a layer with a non quarter-wavelength thickness, or with a different dielectric constant from n_H and n_L. Around the defect mode, there exists resonance inside the defect of the Bragg reflector thus it behaviors like a waveguiding structure.

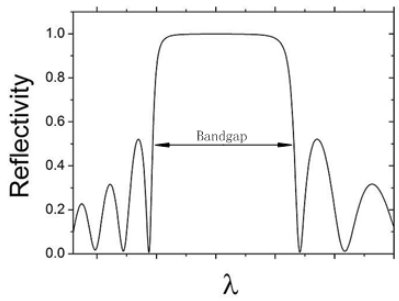

Figure 2.5 Reflectivity spectrum for a Bragg reflector showing the bandgap in which the reflectivity is high and light cannot propagate through the structure [43].

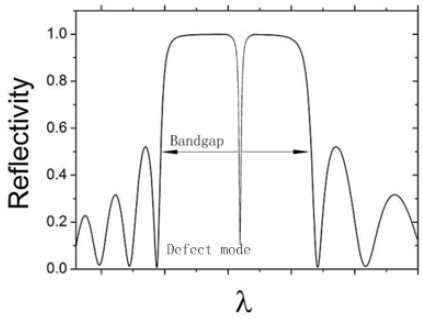

Figure 2.6 Reflectivity spectrum for a Bragg reflector with a defect in the center showing the transmission peak inside the bandgap [43, revised].

As we have discussed in Section 2.3, the effective refractive index of MIM structure depends not only on the dielectric constants of the insulator and the metal, but also on the slit width. Thus, by a similar principle, dielectric modulated plasmonic Bragg reflector and slit width modulated one has been proposed in [28] and [29], respectively.

Compared to the conventional Bragg reflector, plasmonic Bragg reflector shows very similar transmission spectra as shown is Fig. 2.7 and 2.8 [28, 29].

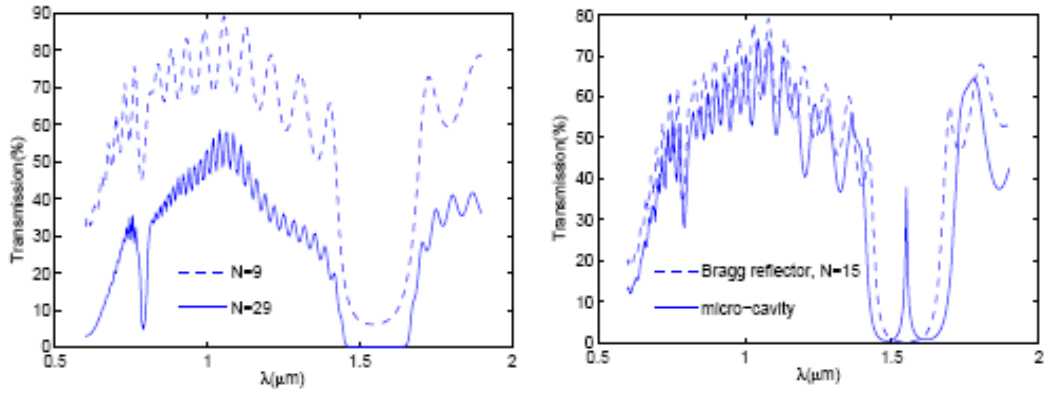

(a) without defect (b) with defect

Figure 2.7 Transmission spectra for dielectric modulated plasmonic Bragg reflectors [28].

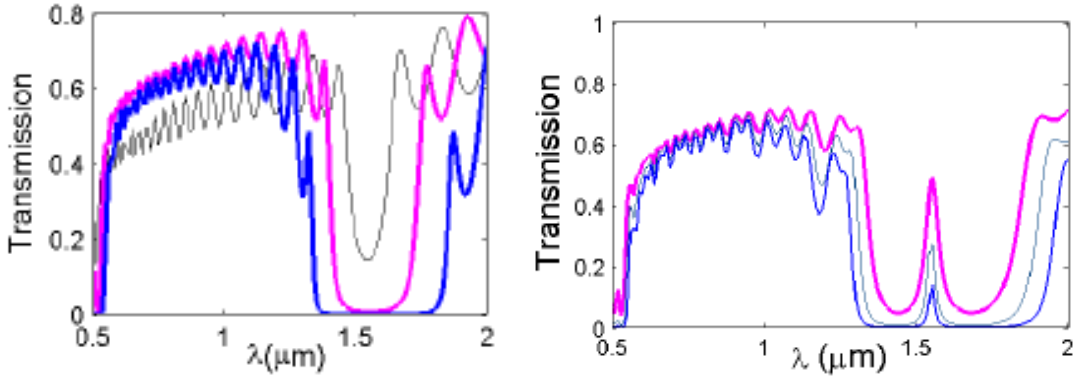

(a) without defect (b) with defect

Figure 2.8 Transmission spectra for slit width modulated plasmonic Bragg reflectors [29].

2.5 Optical switching based on nonlinear Bragg reflectors

When nonlinearity is introduced inside the dielectric material of the $\lambda/4$-shifted Bragg reflector, the change of the input source intensity will lead to the change of the refractive index of the insulator, and hereby the effective refractive indices of MIM structures of the Bragg reflector. Thus the whole transmission spectrum shifts [30] towards longer wavelengths when the source intensity increases, as shown in Fig. 2.9.

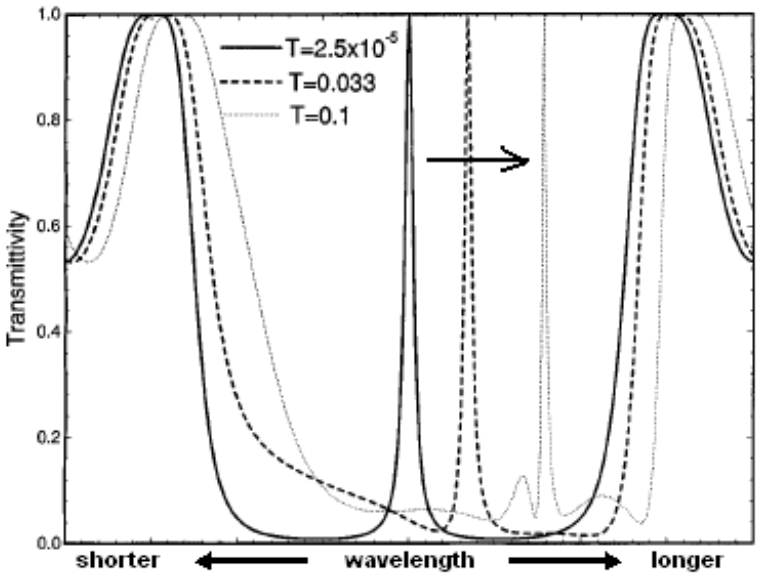

Figure 2.9 The shift of the transmission peak when the source intensity T is increased [30, revised].

Then it is obivious that at a given wavelength near and to the right (i.e. lower frequency) of the transmission peak, the transmission will experience a huge jump when the incident intensity rises to a certain level. And a sharper transmission peak will lead to a more steep jump. Therefore, very small change of the source amplitude will lead to a huge difference of the transmission.

This phenomenon can also be expressed as a hysteresis loop as shown in Fig. 2.10. The input-output characteristics of the nonlinear $\lambda/4$-shifted Bragg reflector can be obtained theorectically [30]. For two different $\Delta\lambda(= \lambda - \lambda_{peak})$, the input-output curves are plotted in Fig. 2.10.

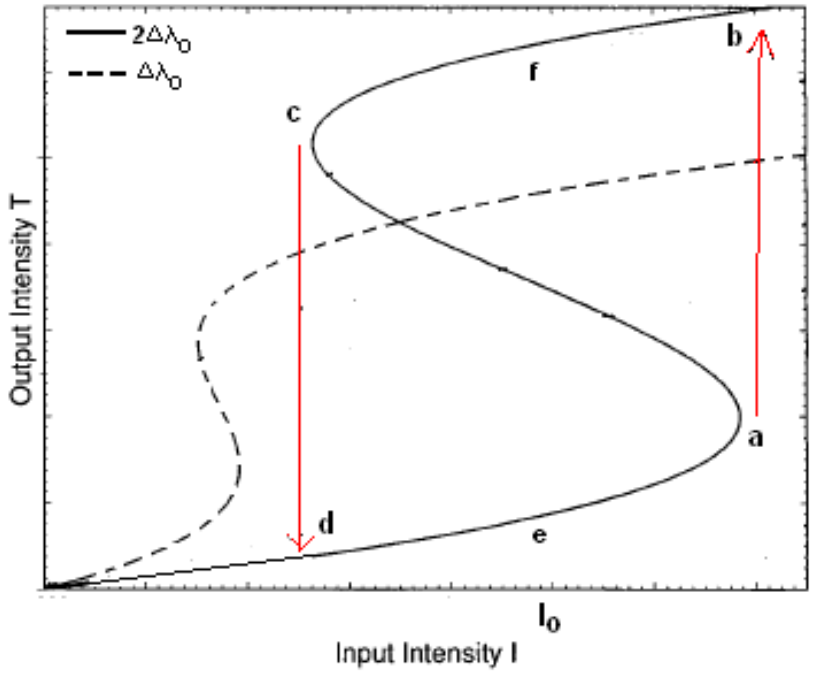

Figure 2.10 Input-output characteristics of nonlinear $\lambda/4$-shifted Bragg reflector [30, revised].

Let's take the longer wavelength (i.e. $\Delta\lambda = 2\Delta\lambda_0$) curve. If the input intensity I is at zero, the corresponding system status is at the origin point. When the system is at a and I still increases, the previously described transmission jump will happen and the system will switch to b. Similarly, when the system is at c and I decreases, a severe transmission fall will happen and the system will switch to d.

Thus the exact system status can not be determined if only the input intensity is given. For example, when $I = I_0$, whether the system is at e or f depends on the history: If the system was previously on the c-b curve, the system status is at f; Otherwise, at e if it was on the d-a curve. This is why it is called as a "hysteresis loop".

This hysteresis property can be used for optical switching with the input intensity I as the control signal. By manipulating the value of I, the system can switch between status e and f either following an $e \to a \to b \to f$ or an $f \to c \to d \to e$ path.

For the wavelength closer to the peak (i.e. $\Delta\lambda = \Delta\lambda_0$), the corresponding hysteresis loop is narrower according to Fig. 2.10.

CHAPTER 3. DESIGN AND SIMULATION METHODOLOGY

3.1 Modeling the metal

As discussed in Chapter 2, Drude model is used to characterize the metal used in this project. Silver(Ag) is chosen as the metal in our MIM structure since it has less damping against the SPP mode , which leads to less energy dissipation in the waveguide. To be more accurate, the parameters in Drude model (which are the plasma frequency ω_p and the damping coefficient Γ) are carefully tuned over the frequency range of interest to fit the measure data by Johnson and Chiristie in 1972 [37]. In the simulation, they are set as $\omega_p = 1.3981 \times 10^{16}$ Hz and $\Gamma = 3.006 \times 10^{13}$ Hz, which yields a good fitting as shown in Fig. 3.1.

3.2 Operating frequency and Bragg section

The operating frequency is set at 1600nm, while 1550nm is the typical operating frequency for many optic devices.

The refractive index of the insulator in the MIM strucure is set as 1.46. Besides SiO_2, a lot of common materials can be processed to have a refractive index near 1.46. In Chapter 2, the relationship between the slit width of the MIM structure and its effective refractive index has been studied. Moveover, some simple numerical methods, such as Transfer Matrix Method(TMM) [48], can be used to calculate the index when the slit width is determined. The results are shown in Fig. 3.2.

The narrow and wide slit width of the Bragg section is chosen as $a = 30$nm and $b = 100$nm. According to Fig. 3.2(a), the corresponding effective index is $n_a = 2.301$ and $n_b = 1.755$. To satisfy the Bragg condition (Eqn. 2.7), the length of each layer is set as $L_1 = 170$nm and

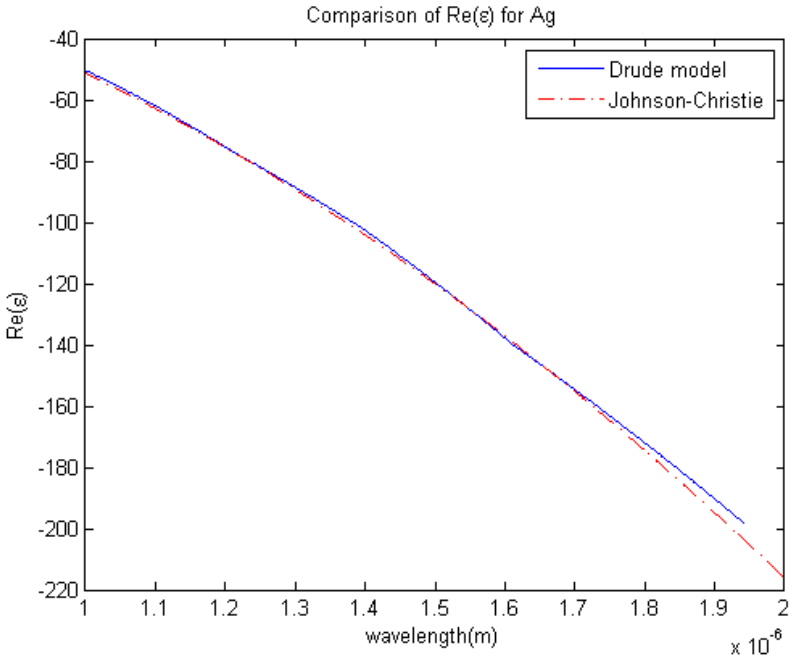

(a) Real Part

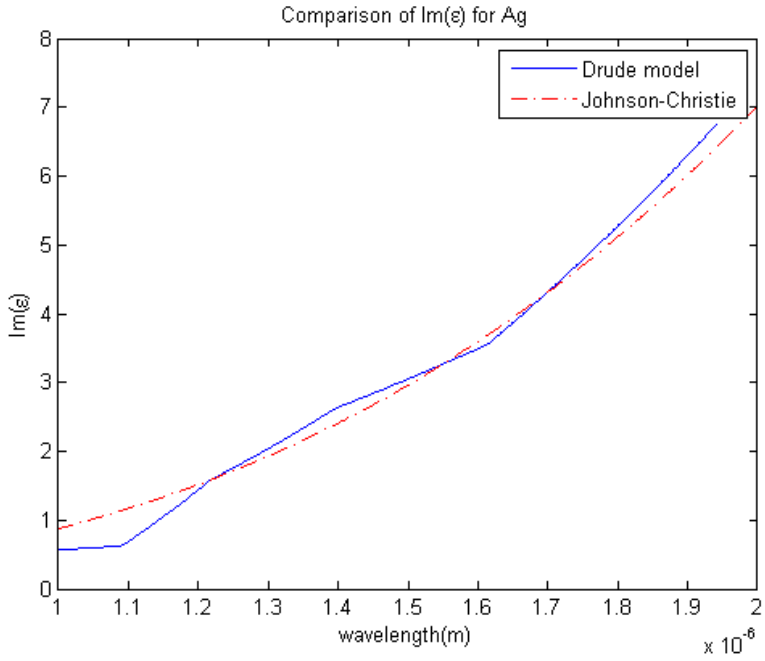

(b) Imaginary Part

Figure 3.1 Comparison of the measured permittivity of Ag [37] and the fitted value of Drude model.

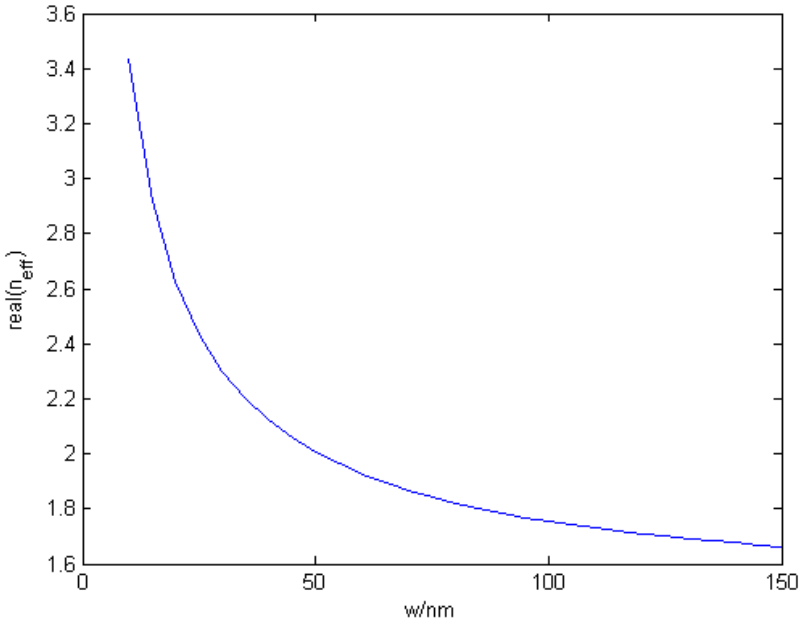

(a) Real Part

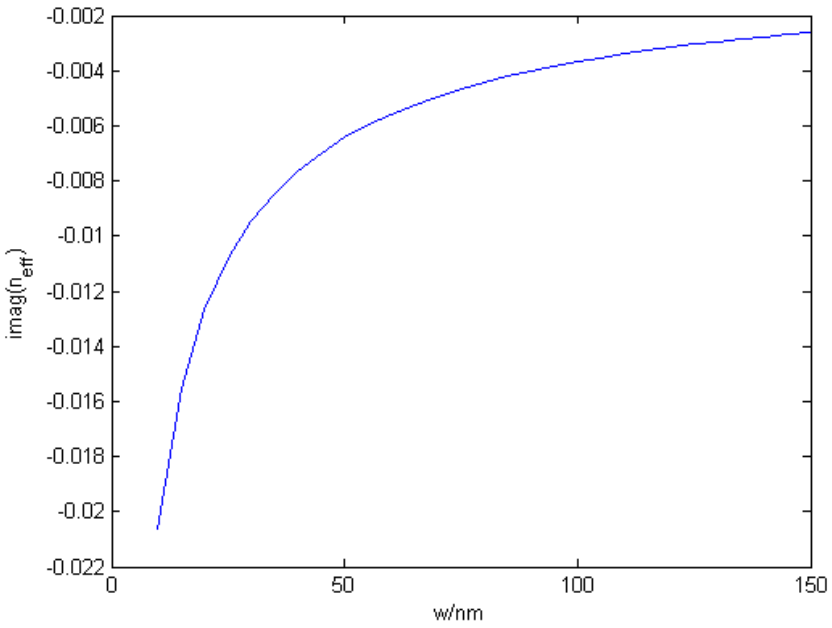

(b) Imaginary Part

Figure 3.2 Calculated effective refractive index vesus the slit width of Ag-SiO_2-Ag MIM structure by Transfer Matrix Method.

$L_2 = 220$nm. The resulting unit Bragg section is as shown in Fig. 3.3(a). An N-layer plasmonic Bragg reflector is shown in Fig. 3.3(b).

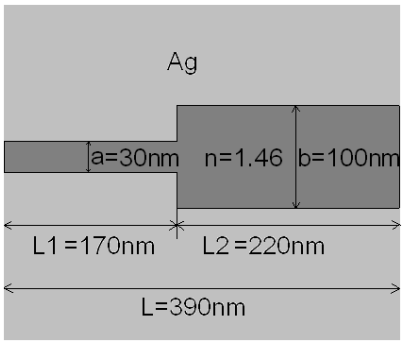

(a) Bragg section

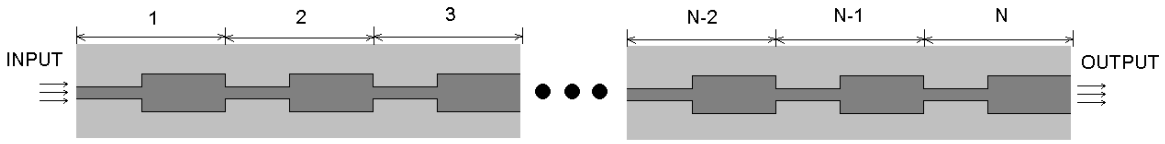

(b) N-layer plasmonic Bragg reflector

Figure 3.3 Plasmonic Bragg reflector.

3.3 Sawtooth plasmonic Bragg reflector

When two MIM structures with different slit widths are connected directly, there exists non-Bragg reflection at the interface and leads to extra energy loss. To confirm this point, a sawtooth variant of the plasmonic Bragg reflector is proposed here.

3.3.1 Structure

Fig. 3.4(a) shows the difference and connection between the original plasmonic Bragg reflector and the sawtooth one. The minimum and maximum slit widths are kept as the same as $a = 30$nm and $b = 100$nm. And the total section length also remains the same as $L = 390$nm. However, instead of abruptly changing from one slit width to the other, the sawtooth structure varies more smoothly. The slit width decreases linearly from b to a, and then increases back to b linearly. Fig. 3.4(b) presents an N-layer sawtooth plasmonic bragg reflector.

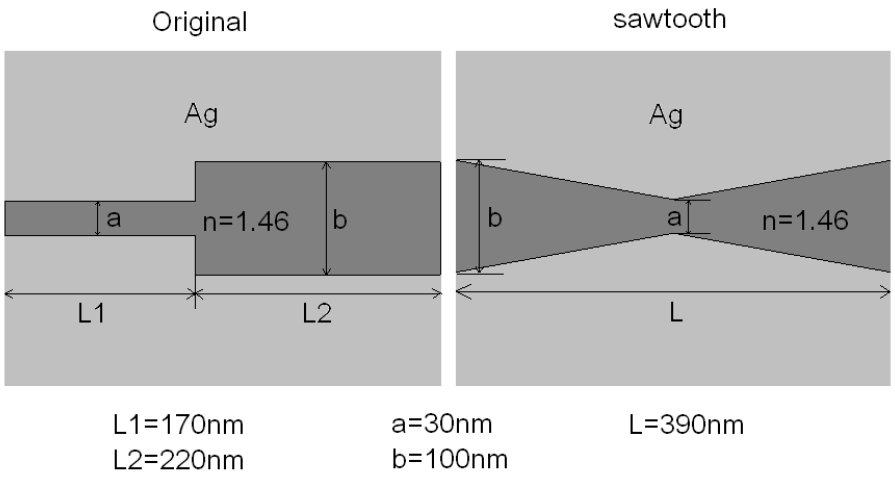

(a) Bragg section & its sawtooth variant

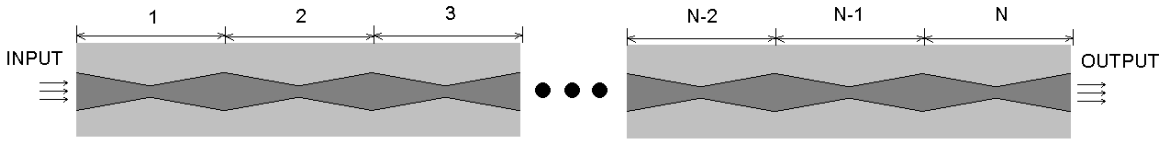

(b) N-layer sawtooth plasmonic Bragg reflector

Figure 3.4 Sawtooth plasmonic Bragg reflector.

3.3.2 Finite Element Method(FEM)

The finite element method is a common numerical technique used originally for solving complex elasticity and structural analysis problems in civil and aeronautical engineering. [49] It was designed to solve both the partial differential equations (PDE) as well as integral equations. It was first developed by Alexander Hrennikoff (1941) and Richard Courant (1942). And it was then widely used in many other engineering areas soon after that, including electromagnetics.

The central idea of this method is mesh discretization of a continuous domain into a set of discrete subdomains, usually called elements, in which the unknown funtion is represented by simple interpolation functions with unknown coefficients. The original problem with infinte number of degrees of freebom, which can be represent as variables in calculations, is converted into a numerically solvable one with finite number of degrees of freedom. Therefore, the accuracy of FEM is very sensitive to the way of discretization. By using a more refined meshing, the obtained structure is more close to the original one. After the discretization,

numerical techniques can be used to solve all the equations, together with the applicable physical constraints.

COMSOL Multiphysics (formerly FEMLAB) is a finite element analysis and solver software package for various physics and engineering applications [50]. In our simulation, COMSOL 3.3 with RF module is used as the FEM tool. The whole modeling procedure contains the following major steps:

1. Modeling of the geometry;
2. Setting of physics conditions such as boundary conditions and subdomain parameters;
3. Meshing;
4. Numerically solving;
5. Postprocessing and visualization.

3.3.3 Simulation

In this thesis, five sawtooth plasmonic Bragg reflectors with different number of layers as N=6,8,10,12,20 are simulated using COMSOL. Meanwhile, plasmonic Bragg reflectors with N=6,8,10,12,20 are also simulated for the comparison need.

3.4 $\lambda/4$-shifted plasmonic Bragg reflector

3.4.1 Structure

The $\lambda/4$-shifted plasmonic Bragg reflector used in the simulation is shown in Fig. 3.5. It contains 6 Bragg sections as in Fig. 3.3(a). The defect in the middle yields a $\lambda/4$ shift, which can be easily achieved by duplicating one single MIM section. Thus the defect length is set as $L_d = 220$nm.

The whole structure is surrounded by perfectly matched layers(PML) in the simulation.

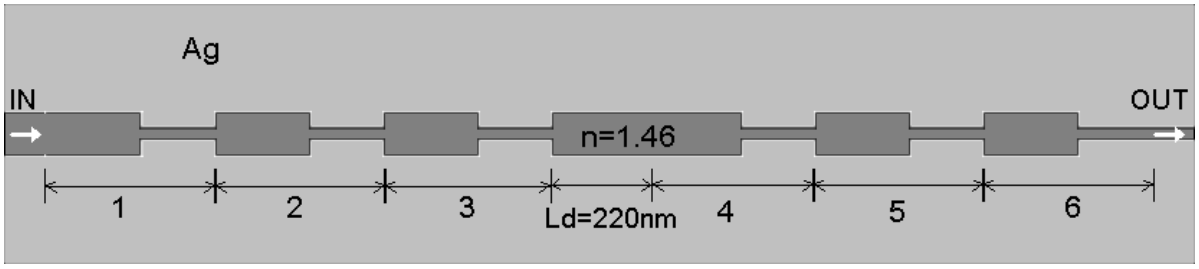

Figure 3.5 6-layer $\lambda/4$-shifted plasmonic Bragg reflector.

3.4.2 Finite-difference time-domain method(FDTD)

Finite-difference time-domain (FDTD) is a popular computational electrodynamics modeling technique. It first discretizes the Maxwell's equations via central difference method in both the time and space domain, and then numerically solving these equations. Since it solves the Maxwell's equations directly, there are nearly no approximations or theoretical restrictions. As a time-domain simulaton method, it can solve over a wide frequency range by only a single simulation run [51].

The essential idea of FDTD was developed by Kane Yee in 1966, when he introduced the famous Yee cell which is shown in Fig. 3.6.

Maxwell's curl equations can be written as six simple scalar equations in Cartesian coordinates, provided that there is no flowing current or isolated charges inside the space domain [52]. The temporal change of the H field is dependent upon the spatial variation of the E field, and vice versa. The vector components of the electric and magnectic fields are arranged alterna-

tively in the cell and satisfy both the differential and integral forms of Maxwell's equations. The equations are then solved in a "leap-frog" manner. All of the electric fields are solved at a given time instance using magnetic fields obtained at a previous instance. Then all the magnetic fields are solved using the newly obtained electric fields. By repeating such a process, the evolution of all the fields can be obtained over the time domain.

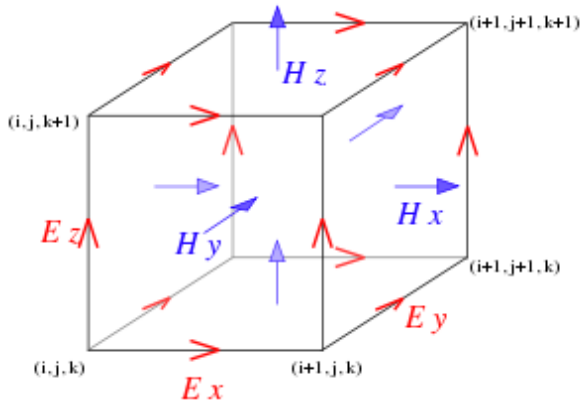

Figure 3.6 Illustration of a standard Cartesian Yee cell used for FDTD, about which electric and magnetic field vector components are distributed (Yee 1966) [53].

3.4.3 MIT Electromagnetic Equation Propagation(MEEP)

3.4.3.1 Introduction

MIT Electromagnetic Equation Propagation(MEEP) is a free FDTD simulation software package developed at MIT to model electromagnetic systems [54]. It offers many feathers and complete scriptability. All the FDTD simulations in this project use MEEP as the back-end FDTD calculation library.

3.4.3.2 Units in MEEP

MEEP uses dimensionless units. Because Maxwell's equations are scale invariant [55], it is convenient in electromagnetic problems to choose scale-invariant units. In MEEP, nearly all the optic constants like ϵ_0,μ_0 and c are unity.

Therefore, it is reasonable to specify parameters in a dimensionless way. In particular, Kerr nonlinearities need a detailed explanation here.

Instantaneous Kerr nonlinearities is defined to be characterized by a susceptibility $\chi^{(3)}$. However, the strength of the Kerr nonlinearity is usually specified as the AC Kerr coefficient n_2. Let I represent the time-average intensity of a planewave travelling through a homogeneous Kerr material. Then the following relationship exists between these variables as [56]:

$$n = n_0 + \frac{3\chi^{(3)}}{8n_0} |\mathbf{E}_\omega|^2 = n_0 + n_2 I \tag{3.1}$$

where n and n_0 are the intensity dependent and linear refractive index.

Thus in the nonlinear calculations in MEEP, only the product $n_2 I$ is useful. The value of n_2 and I in SI units is not important. Therefore, the value of $n_2 I$ instead of the incident intensity or the susceptibility is specified and reported in MEEP.

For the results, as transmission is expressed as a ratio of transmitted to incident intensities, the units of fields are irrelevant. Although all the fields are in MEEP units in the results, the conversion of units is not necessary as transmission has the same value under both the unit systems.

3.4.3.3 Modeling metal in MEEP

Physically, material dispersion exists due to that the polarization of the material does not respond intantaneously to an applied external field $\mathbf{E}$. In MEEP, $\mathbf{D} = \epsilon\mathbf{E}$ is expanded to [57]:

$$\mathbf{D} = \epsilon_\infty \mathbf{E} + \mathbf{P} \tag{3.2}$$

where ϵ_∞ is the instantaneous dielectric function and $\mathbf{P}$ is the remaining frequency-dependent polarization density in the material. $\mathbf{P}$ has its own time-evolution equation, and the exact form of this equation determines the frequency-dependence $\epsilon(\omega)$. In particular, MEEP supports any material dispersion of the form of a sum of harmonic resonances as below [57]:

$$\epsilon(\omega, x) = \epsilon_\infty(x) + \sum_n \frac{\sigma_n(x) \cdot \omega_n^2}{\omega_n^2 - \omega^2 - i\omega\gamma_n} \tag{3.3}$$

where ω_n and γ_n are user-specified constants, and the $\sigma_n(x)$ is a user-specified function of position giving the strength of the n-th resonance.

In order to model metal using the Drude model, ω_n is set as a very small value and $\sigma_n(x)$ is set to make $\sigma_n(x) \cdot \omega_n^2$ equal to ω_p^2 in Eqn. 2.1. Then obiviously, γ_n is equivalent to the damping coefficent Γ. By this way, the Drude model is represent as a harmonic resonance in MEEP.

3.4.3.4 Scripting front-ends

MEEP offers two programming interfaces: C++ and Scheme.

However, both of them lack the following essential features:

- Interactive job control: the ability to stop/pause/resume during the simulation by external signals(e.g. keystrokes).
- Interactive in-simulation input/output: the ability to exchange information at any time during the simulation.
- Script reusability: Object Oriented style interface to avoid scripting routines in each single script file.

In our project, GNU Ncurses package and self-developed Application Programming Interfaces(APIs) are used as solutions to these drawbacks.

3.4.3.5 Parallel computation

Since FDTD requires the entire computational domain be gridded and the spatial discretization grid must be sufficiently small to resolve both the smallest electromagnetic wavelength and the smallest geometrical unit in the model [51], along with MEEP's isotropic meshing policy, our FDTD simulations require excessive computation resources for single PCs. The typical runing time is about 10 hours for a single simulation.

As MEEP supports MPI based parallel computation, it was successfully ported to the Mountain cluster in ECpE department of Iowa state university. The MPI implementation on

Mountain is MPICH. The typical running time on the cluster is about 1 hour for a single simulation.

3.4.4 Simulation

The following FDTD simulations are performed in this project:

- Tranmission spectra for linear $\lambda/4$-shifted plasmonic Bragg reflector (in order to determine the position and the shape of the transmission peak inside the stop band).
- Hysterisis loops at two frequencies for nonlinear $\lambda/4$-shifted plasmonic Bragg reflector.
- Optical switching using a continuous source.
- Optical switching using a pulse source.

CHAPTER 4. RESULTS AND ANALYSES

4.1 Sawtooth plasmonic Bragg reflector

The obtained transmission spectra of plasmonic Bragg reflector and its sawtooth variant is shown as below in Fig. 4.1 and Fig. 4.2.

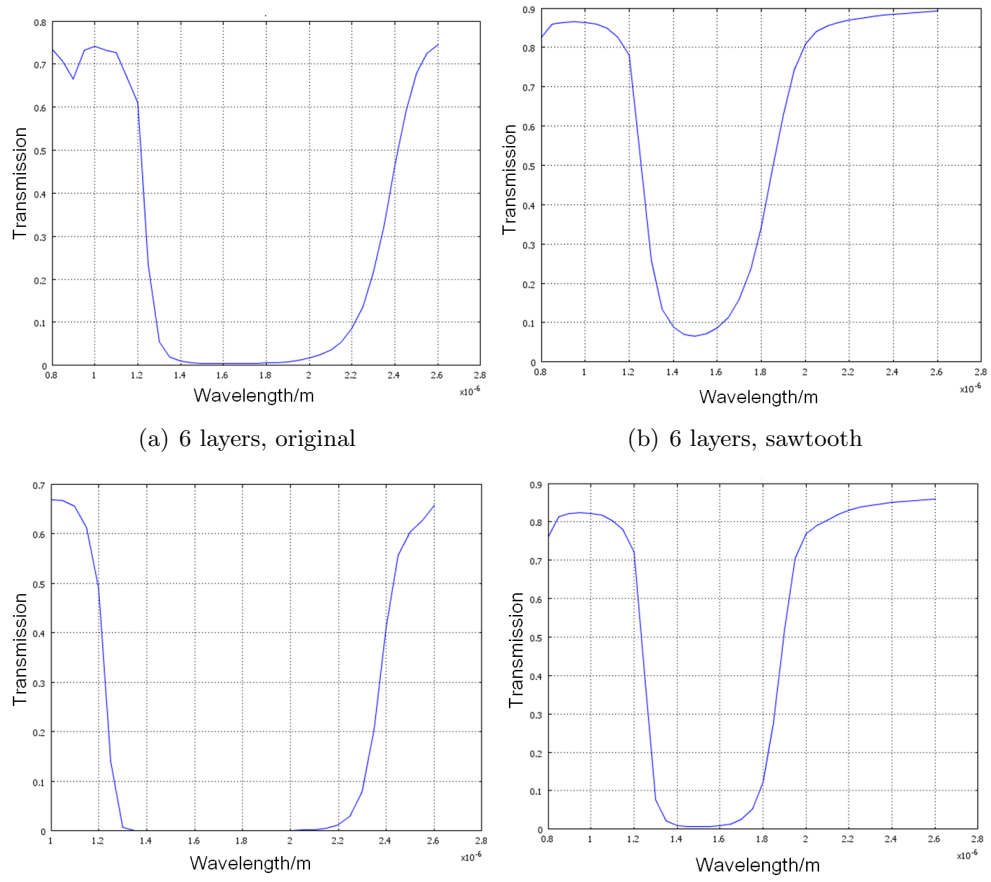

(a) 6 layers, original

(b) 6 layers, sawtooth

(c) 8 layers, original

(d) 8 layers, sawtooth

Figure 4.1 Transmission comparison of plasmonic bragg reflector and its sawtooth variant, for N=6,8.

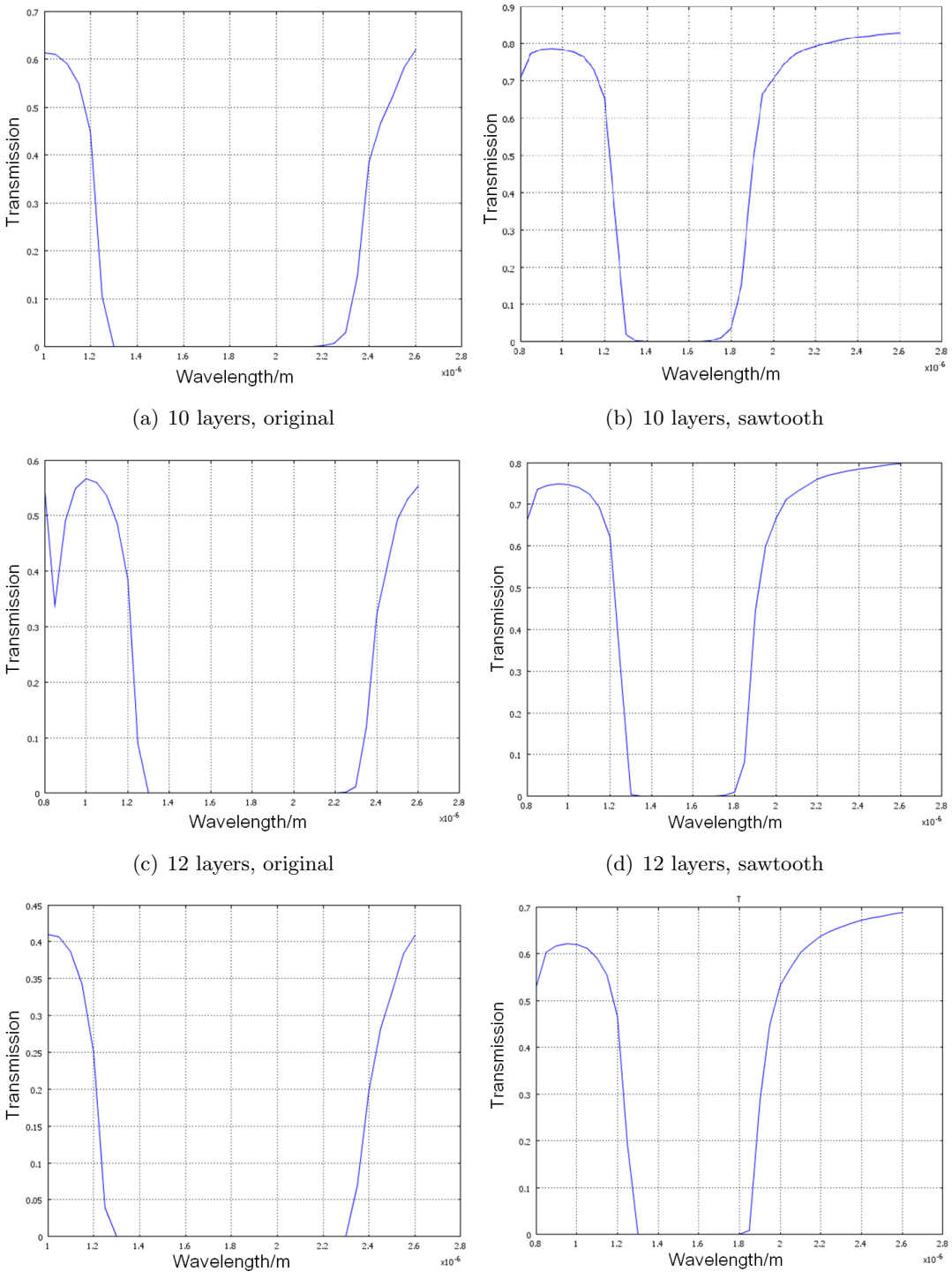

(a) 10 layers, original

(b) 10 layers, sawtooth

(c) 12 layers, original

(d) 12 layers, sawtooth

(e) 20 layers, original

(f) 20 layers, sawtooth

Figure 4.2 Transmission comparison of plasmonic bragg reflector and its sawtooth variant, for N=10,12,20.

In order to get a better illustration of the advantage of the sawtooth structure, the transmission at a fixed frequency $\lambda = 1000$nm is plotted in Fig. 4.3 as below. From Fig. 4.1 and Fig. 4.2, it's very obivious that 1000nm is the just at the edge of the left pass band.

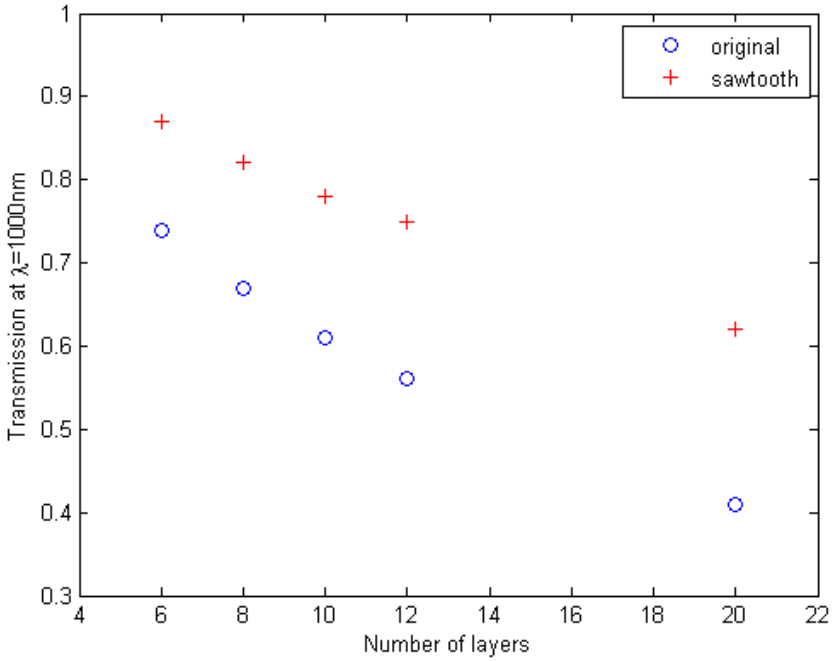

Figure 4.3 Transmission at $\lambda = 1000$nm for plasmonic bragg reflector and its sawtooth variant.

Fig. 4.3 demonstrates that the sawtooth structure not only has a higher transmission comparing to the original plasmonic Bragg reflector, which confirms that the sawtooth structure reduces the energy loss due to the mode mismatching, but also has a less decreasing rate of the transmission when more layers are added. Therefore, for the 20-layer configuration, the sawtooth structure yields a 50% higher transmission. This is a great advancement as 6-layer sawtooth structure only has a 18% lead of the transmission. Thus, the band edge becomes more shaper when the layer number increases for the sawtooth structure. Fig. 4.2(f) shows that, at the band edge, the transmisson of the 20-layer sawtooth structure drops from 45% to zero when the wavelength changes from 1200nm to 1300nm, which is a 45%/100nm change rate. However, for the 20-layer orignial structure, it's only 24%/100nm as shown in Fig. 4.2(e).

This characteristic makes the sawtooth structure also a good candidate for optical switching via band edge tuning [30].

Fig. 4.1 and Fig. 4.2 also indicates that the sawtooth structure has a narrower stop band. This characteristic, along with the sharp band edge property, reveals the possible application for constructing band-stop filters. And, the smoothier change along the metal-insulator interface reduces fabrication difficulty of the sawtooth structure compared to the original one.

4.2 $\lambda/4$-shifted plasmonic Bragg reflector

For time-domain methods(e.g. FDTD), solutions can cover a wide frequency range with a single simulation run. Using a single gaussian source as the input, the transmission spectra of the linear $\lambda/4$-shifted plasmonic Bragg reflector is obtained by a single FDTD simluation. The result is plotted in Fig. 4.4 as below:

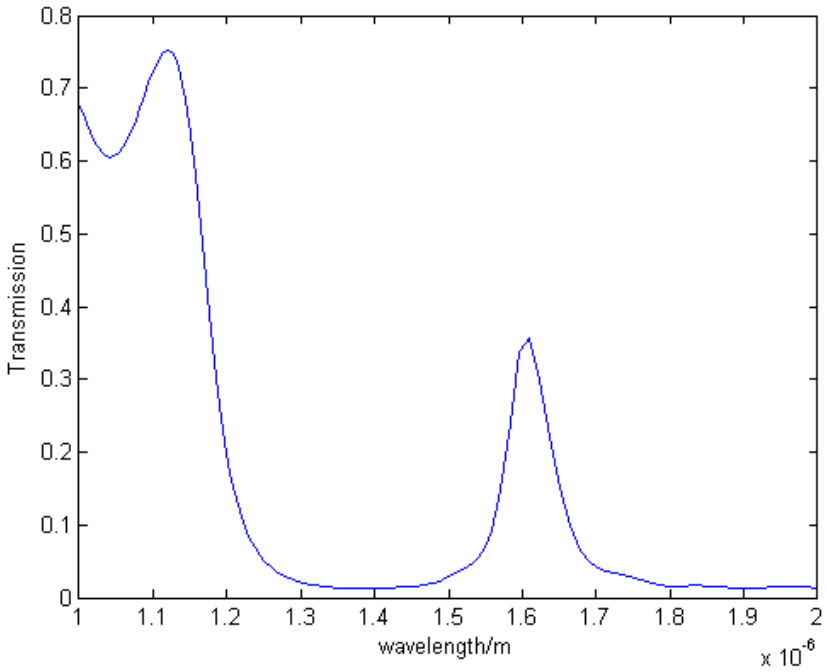

Figure 4.4 Transmission spectra of linear $\lambda/4$-shifted plasmonic Bragg reflector.

Thus, for the proposed structure, the transmission at the peak is about 37% at $\lambda = 1600$nm, while the minimum transmission inside the stop band is only about 2% at the frequency around 1400nm.

To get the field distribution inside the reflector, the continuous single-frequency source, instead of the previous gaussion source is used in the simulation. The **Hz** field patterns at the frequencies of 1400nm and 1600nm are illustrated in Fig. 4.5.

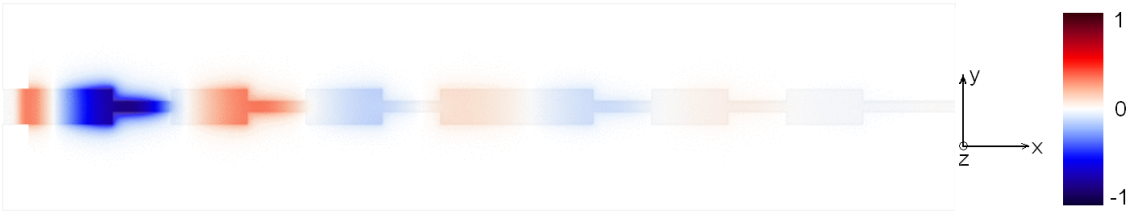

(a) $\lambda = 1400$nm, inside the stop band

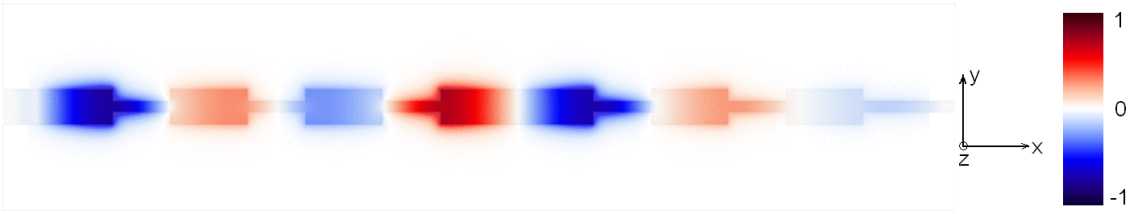

(b) $\lambda = 1600$nm, at the transmission peak

Figure 4.5 The field distribution of **Hz** inside the reflector at $\lambda = 1400$nm and $\lambda = 1600$nm, respectively.

At $\lambda = 1600$nm, it's very clear that there exists strong resonance inside the defect. As already dicussed in Chapter 2, this is the underlying reason for the transmission peak.

4.2.1 Hysteresis loops

Two sets of simulations are performed for two frequencies: 1660 and 1700nm. The obtained hysteresis loops are plotted in Fig. 4.6 and 4.7. Each circle (red or blue) represents the result of one single simulation.

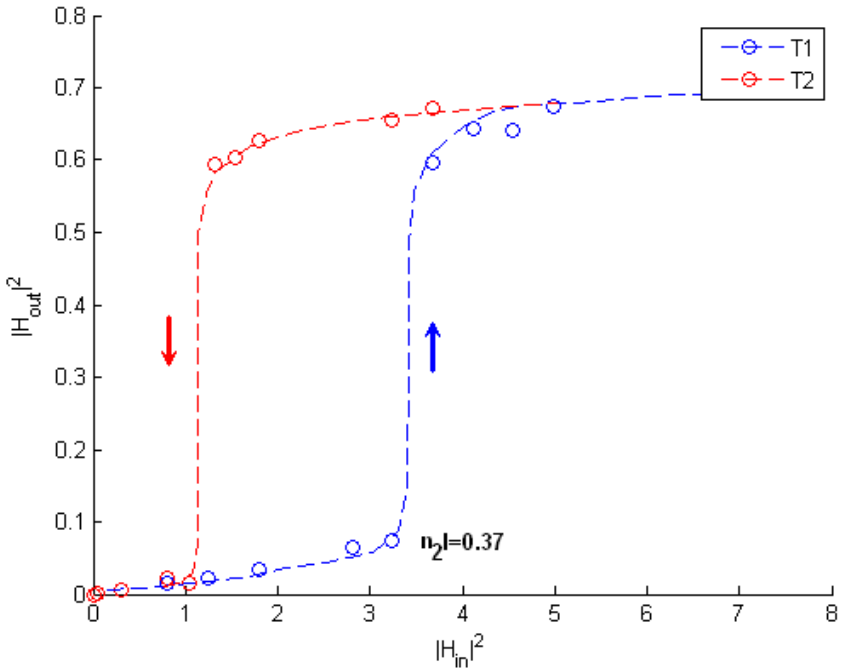

Figure 4.6 Output-input intensity relation of nonlinear $\lambda/4$-shifted plasmonic Bragg reflector at the frequency of $\lambda = 1660$nm. T1 and T2 denote the transmissions respective obtained from increasing and decreasing intensity of incident light.

From Fig. 4.6, the switching-up source intensity at $\lambda = 1660$nm is $n_2 I = 0.37$. According to Section 2.5, this hysteresis loop should be narrower compared to the one at $\lambda = 1700$nm.

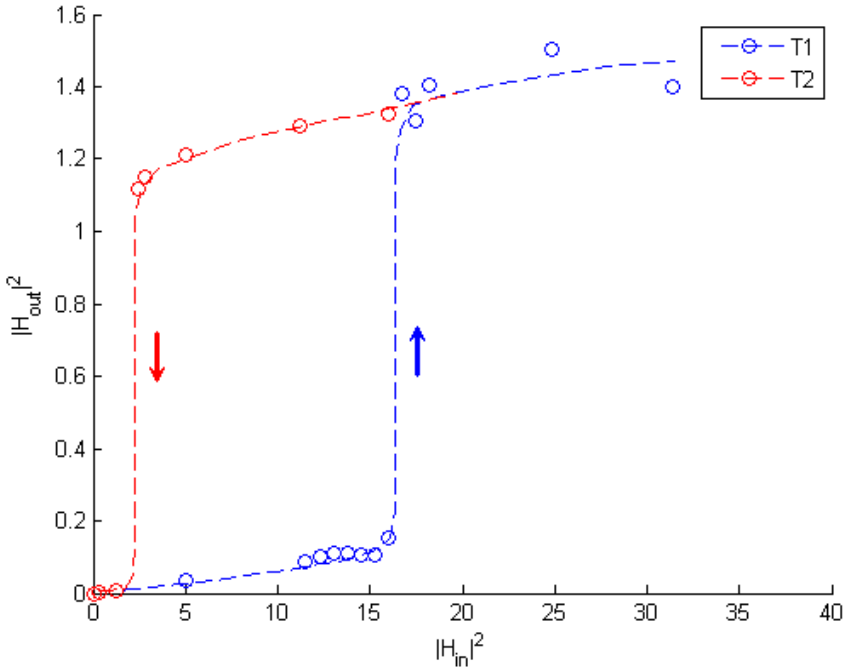

Figure 4.7 Output-input intensity relation of nonlinear $\lambda/4$-shifted plasmonic Bragg reflector at the frequency of $\lambda = 1700$nm. T1 and T2 denote the transmissions respective obtained from increasing and decreasing intensity of incident light.

From Fig. 4.7, the switching-up source intensity at $\lambda = 1700$nm is $n_2 I = 1.69$. Although the switching-up power is much higher, this hysteresis loop is much wider. Thus it will have better stability if used for optical memory devices, while the 1600nm configuration yields less power consumption.

4.2.2 Optical switching using a continuous source

Fig. 4.8 shows the switching process under $\lambda = 1700$nm.

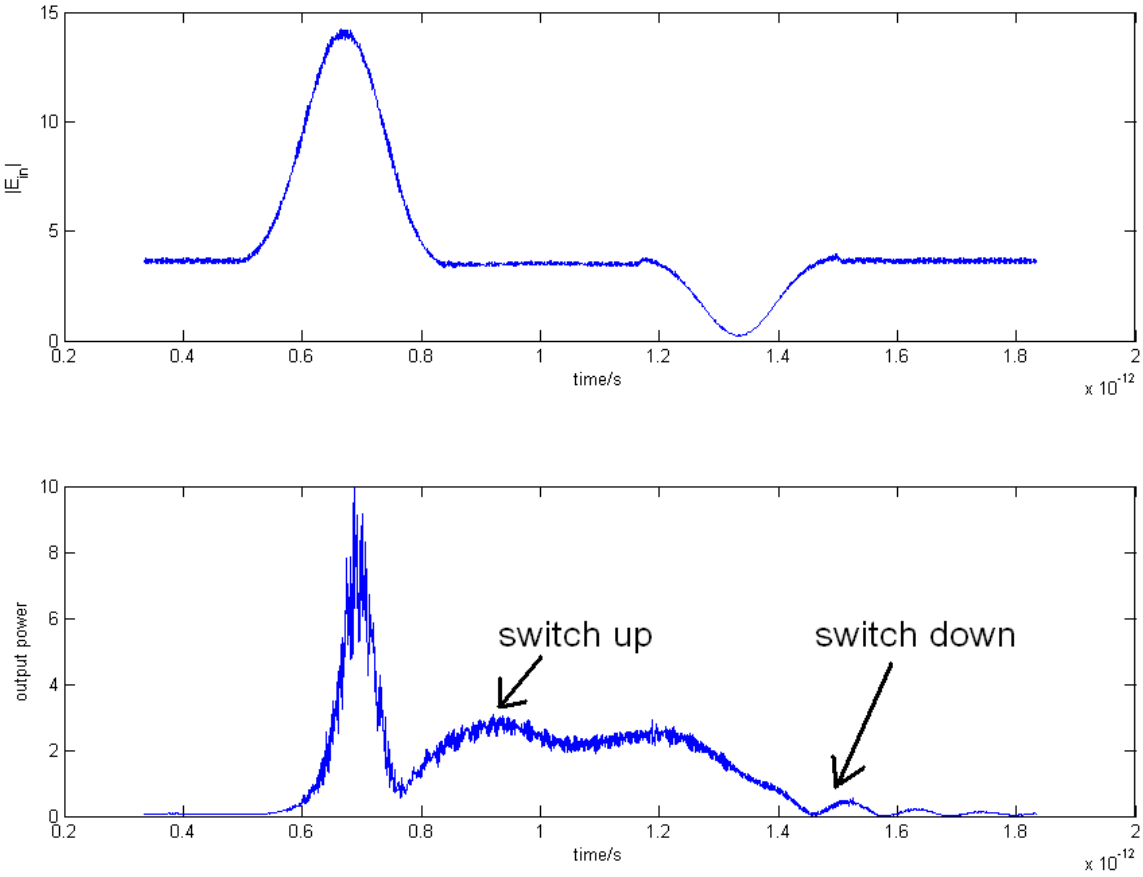

Figure 4.8 Source amplitude (up) and output power (down) vesus time showing the switching process of nonlinear $\lambda/4$-shifted plasmonic Bragg reflector at the frequency of $\lambda = 1700$nm.

In order to get the switch time delay, switch-up and switch-down processes are simulated seperately. The results are shown in Fig. 4.9 and 4.10, respectively.

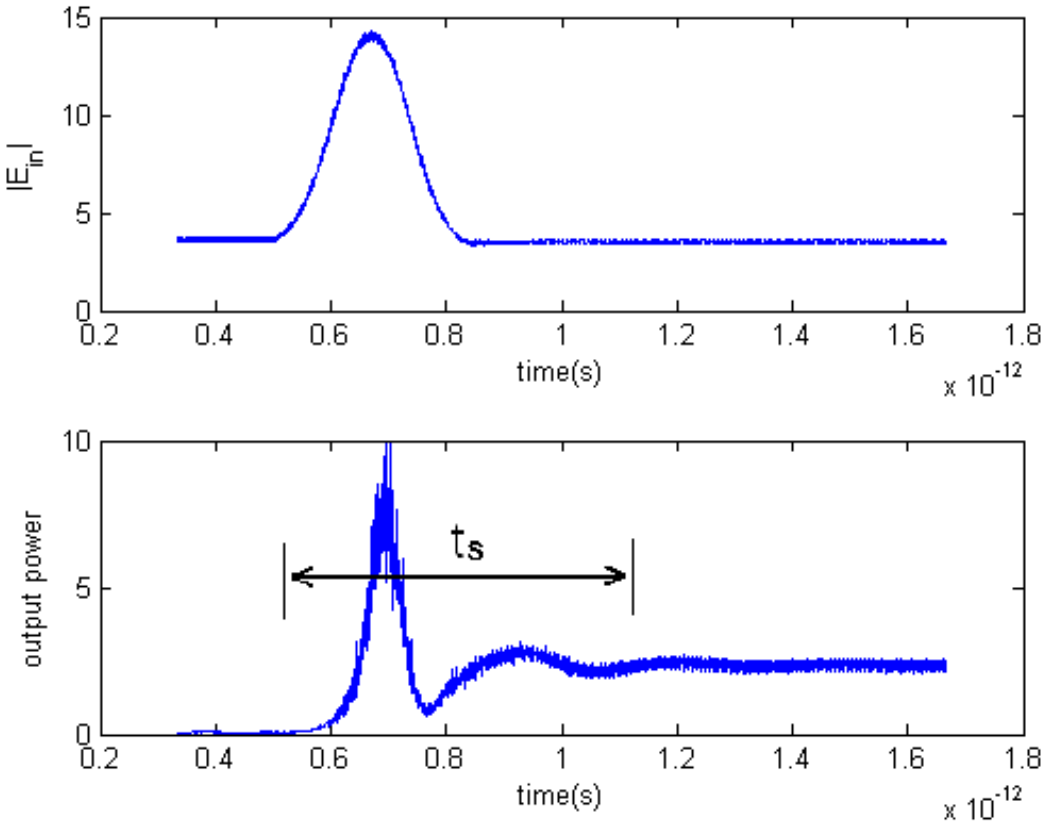

Figure 4.9 Source amplitude (up) and output power (down) vesus time showing the switch-up process of nonlinear $\lambda/4$-shifted plasmonic Bragg reflector at the frequency of $\lambda = 1700$nm.

The switch-up time delay t_s is less than 0.6×10^{-12}s.

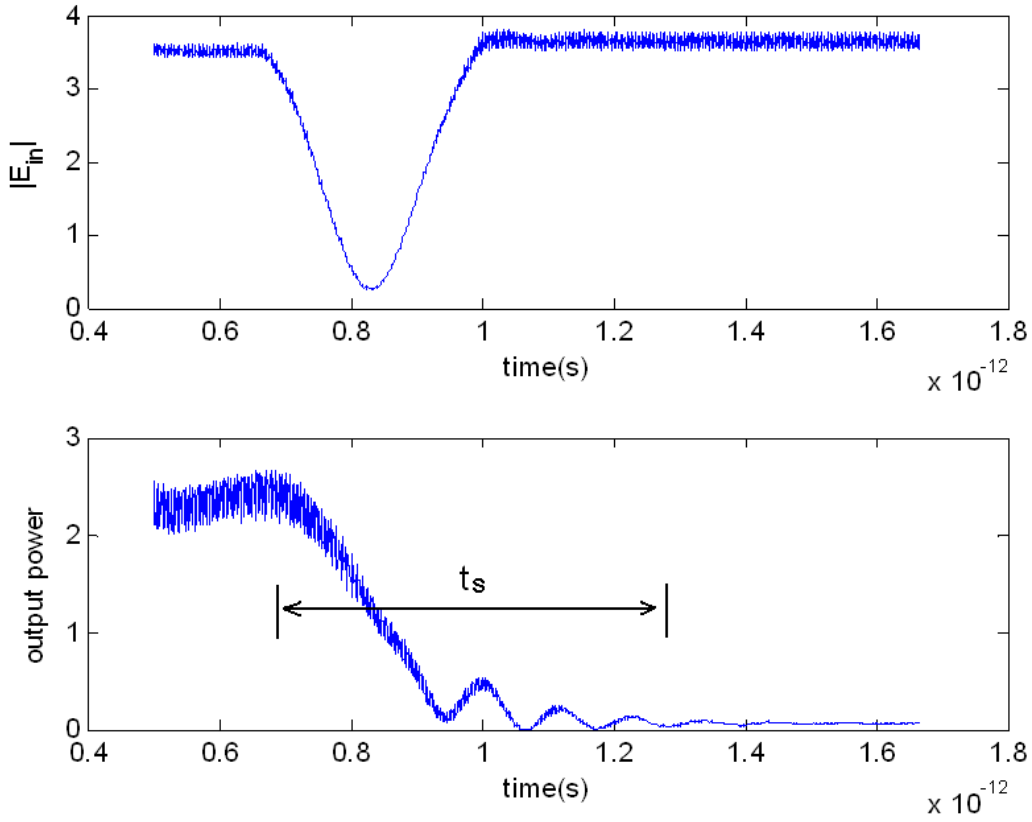

Figure 4.10 Source amplitude (up) and output power (down) vesus time showing the switch-down process of nonlinear $\lambda/4$-shifted plasmonic Bragg reflector at the frequency of $\lambda = 1700$nm.

The switch-down time delay t_s is also less than 0.6×10^{-12}s.

4.2.3 Optical switching using a pulse source

Fig. 4.11 shows the switching result using a pulse source at $\lambda = 1700$nm.

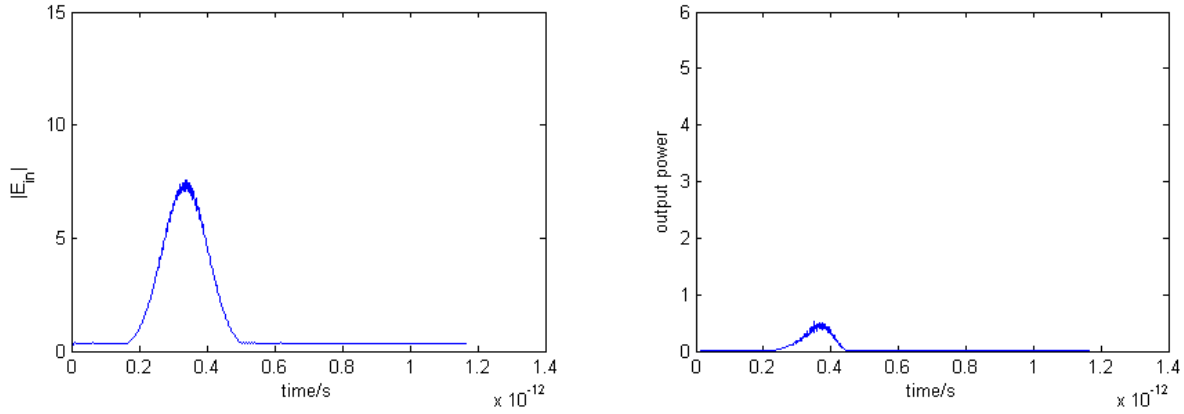

(a) Source amplitude (up) and output power (down) vesus time with a pulse source of intensity I

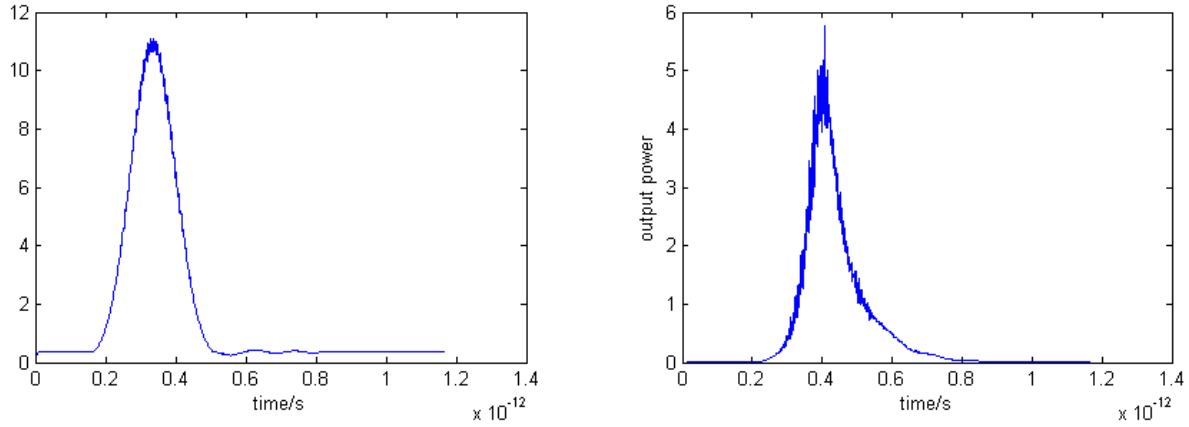

(b) Source amplitude (up) and output power (down) vesus time with a pulse source of intensity 2I

Figure 4.11 Nonlinear $\lambda/4$-shifted plasmonic Bragg reflector with a pulse source at the frequecy of $\lambda = 1700$nm.

Although the input pulse intensity in Fig. 4.11(b) is only twice as that in Fig. 4.11(a), the output power is about 10 times. This is because the switching-up power rests inside the $[I, 2I]$ interval. This result reveals the possible application on optic digital gates although some essential aspects (e.g. timing) still need more considerations.

CHAPTER 5. Summary

This thesis shows some important characteristics of plasmonic Bragg reflectors and their applications on optical switching.

- Sawtooth plasmonic Bragg reflector can effectively reduce the extra energy loss due to MIM mode mismatching. For the applications where remaining a certain level of transmission outside the stop band is necessary, Sawtooth plasmonic Bragg reflector is a better choice. Its sharper band edge can be used to build corresponding filters. The 45%/100nm transmission variation rate also make it a promising nominate for optical switching by tuning at the band edge. More importantly, its fabrication is easier compared to that of the slit width modulated plasmonic Bragg reflector.

- $\lambda/4$-shifted plasmonic Bragg reflector with a defect in the center demonstrates similar properties as its electronic counterpart. Nonlinear $\lambda/4$-shifted plasmonic Bragg reflector presents very good performance on optical switching with switching power as low as $n_2 I = 0.37$ and switch time delay as short as $6ps$. The hysteresis loop of its input-ouput curve offers a possible application on optic memory devices.

Self-developed MEEP APIs can serve as an effective assistant for future FDTD simulations.

BIBLIOGRAPHY

[1] Ozbay E. (2006). Plasmonics: merging photonics and electronics at nanoscale dimensions. *Science*, *311*, 189-193.

[2] Pavesi, L. , Guillot, G. (2006). *Optical Interconnects: The Silicon Approach*. New York: Springer.

[3] Kimerling, L. C. (2000). Silicon microphotonics. *Applied Surface Science*, *8-13*, 159-160.

[4] Kubacki, R. M. (2006). Monolithic integration of microphotonics with CMOS microelectronics using molecularly engineered materials and nanostructures. *Electronic Components and Technology Conference*, 776-781,

[5] Chakraborty, R. (2001). Integrated optical waveguides in LiNbO : Modeling and experimental analysis. *Proc. SPIE-Int. Soc. Optical Engineering*, *4417*, 278-285.

[6] Wikipedia. (2009). Photonic integrated circuit. *Wikipedia, The Free Encyclopedia*. Retrieved June 18, 2009, from http://en.wikipedia.org/w/index.php?title=Photonic_integrated_circuit&oldid=297246136

[7] Eldada, L. A. (2002). Polymer integrated optics: Promise versus practicality. *Proc. SPIE-Int. Soc. Optical Engineering*, 11-22.

[8] Mentzer, M. A. (1990). *Principles of Optical Circuit Engineering*. New York: CRC Press.

[9] Hunsperger, R. G. (2002). *Integrated Optics: Theory and Technology* New York: Springer.

[10] Tien, P. K. (1977). Integrated optics and new wave phenomena in optical waveguides. *Review of Modern Physics*, *49*(2), 361-420.

[11] Ahn, D. , Hong, C. , Liu, J. (2007). High performance, waveguide integrated Ge photodetectors. *Optics Express*, *15*(7), 3916-3921.

[12] Fang, A. W. , Jones, R. , Park, H. , et al. (2007). Integrated AlGaInAs-silicon evanescent race track laser and photodetector. *Optics Express*, *15*(5), 2315-2322.

[13] Wooten, E. L. , Kissa, K. M. , Yi-Yan, A. , et al. (2000). A review of Lithium niobate modulators for fiber optic communications systems. *IEEE J. Sel. Top. Quantum Electron.*, *6*, 69.

[14] Kim, W. , Kwon, S. , Jeong, W. , et al. (2009). Integrated optical modulator for signal upconversion over radio-on-fiber link. *Optics Express*, *17*(4), 2638-2645.

[15] Rong, H. , Kuo, Y. , Xu, S. , et al. (2006). Monolithic integrated Raman silicon laser. *Optics Express*, *14*(15), 6705-6712.

[16] Wiersma, D. S. (2008). Nonlinear optics: Controlling photons with light. *Nature Photonics*, *2*, 136-137.

[17] Asakawa, K. , Sugimoto1, Y. , Watanabe, Y. , et al. (2006). Photonic crystal and quantum dot technologies for all-optical switch and logic device. *New Journal of Physics*, *8*(208).

[18] Shinya, A. , Tanabe, T. , Kuramochi, E. , et al. (2005). All-optical switch and digital light processing using photonic crystals. *NTT Technical Review*, *3*(12).

[19] Wang, F. , Yang, J. , Chen, L. , et al. (2006). Optical switch based on multimode interference coupler *IEEE Photonic Technology Letters*, *18*(2), 421-423.

[20] Dubas, S. T. , Pimpan, V. (2008). Optical switch from silver nanocomposite thin films. *Materials Letters*, *62*, 3361-3363.

[21] Moskovits, M. (2005). Surface-enhanced Raman spectroscopy: a brief retrospective. *J. Raman Spectrosc.*, *36*, 485-496.

[22] Willets, K. A. , Van Duyne, R. P. (2007). Localized surface plasmon resonance spectroscopy and sensing. *Annual Review of Physical Chemistry*, *58*, 267-297.

[23] Homola, J. , Yee, S. S. , Gauglitz, G. (1999). Surface plasmon resonance sensors: review. *Sensors & Actuators: B. Chemical*, *54*, 3-15.

[24] Shalaev, V. M. (2007). Optical negative-index metamaterials. *Nature Photonics*, *1*, 41-48.

[25] Ishimaru, A. , Jaruwatanadilok, S. , Kuga, Y. (2005). Generalized surface plasmon resonance sensors using metamaterials and negative index materials. *Progress In Electromagnetics Research*, *51*, 139-152.

[26] Barnes, W. L. , Dereux, A. , Ebbesen, T. W. (2003). Surface plasmon, subwavelength optics. *Nature*, *424*(14), 824-830.

[27] Zia, R. , Selker, M. D. , Catrysse, P. B. , et al. (2004). Geometries and materials for subwavelength surface plasmon modes. *J. Opt. Soc. Am. A*, *21*(12), 2442-2446.

[28] Hosseini, A. , Massoud, Y. (2006). A low-loss metal-insulator-metal plasmonic bragg reflector. *Optics Express*, *14*(23), 11318-11323.

[29] Liu, J. , Wang, L. , He, M. (2008). A wide bandgap plasmonic Bragg reflector. *Optics Express*, *16*(7), 4888-4894.

[30] Radic, S. , George, N. , Agrawal, G. P. (1995). Theory of low-threshold optical switching in nonlinear phase-shifted periodic structures. *J. Opt. Soc. Am. B*, *12*(4), 671-680.

[31] Hardinga, P. J. , Euser, T. G. , et al. (2007). Dynamical ultrafast all-optical switching of planar GaAs/AlAs photonic microcavities. *Applied Physics Letters*, *91*(111103).

[32] Shen, Y. , Wang, G. P. (2008). Optical bistability in metal gap waveguide nanocavities. *Optics Express*, *16*(12), 8421-8426.

[33] Drude, P. (1900). Zur Elektronentheorie der metalle. *Annalen der Physik*, *306*(3), 566.

[34] Drude, P. (1900). Zur Elektronentheorie der Metalle; II. Teil. Galvanomagnetische und thermomagnetische Effecte. *Annalen der Physik*, *308*(11), 369.

[35] Wikipedia. (2009). Drude model. *Wikipedia, The Free Encyclopedia*. Retrieved June 18, 2009, from http://en.wikipedia.org/w/index.php?title=Drude_model&oldid=297206693

[36] Ashcroft, N. W. , Mermin, N. D. . (1976). *Solid State Physics*, Orlando: Harcourt, Inc.

[37] Johnson, P. B. , Christy, R. W. (1972). Optical constants of the noble metals. *Physical Review B*, *6*(12), 4370-4379

[38] Skullsinthestars. (2008). Measuring neural activity using surface plasmons. *Skull in the Stars*. Retrieved May 12, 2008, from http://skullsinthestars.com/2008/05/12/measuring-neural-activity-using-surface-plasmons/

[39] Wikipedia. (2009). Surface plasmon resonance. *Wikipedia, The Free Encyclopedia*. Retrieved June 22, 2009, from http://en.wikipedia.org/w/index.php?title=Surface_plasmon_resonance&oldid=297999361

[40] Grote, R. (2008) *Design and Application of Plasmonic Devices*. Unpublished master's thesis, Drexel University, Philadelphia.

[41] Miyazaki, H. T. (2006). Squeezing visible lightwaves into a 3-nm-thick and 55-nm-long plasmon cavity. *Physical Review Letters*, *96*(097401).

[42] Han, Z. , Forsberg, E. , He, S. (2007). Surface plasmon Bragg gratings formed in metal-insulator-metal waveguides. *IEEE Photonics Technology Letters*, *19*(2), 91-93.

[43] Wikipedia. (2009). Distributed Bragg reflector. *Wikipedia, The Free Encyclopedia*. Retrieved July 3, 2009, from http://en.wikipedia.org/w/index.php?title=Distributed_Bragg_reflector&oldid=300011998

[44] Gilles, L. , Tran, P. (2002). Optical switching in nonlinear chiral distributed Bragg reflectors with defect layers. *J. Opt. Soc. Am. B*, *19*(4), 630-639.

[45] Morthier, G. , Moeyersoon, B. , Baets, R. (2001). A $\lambda/4$-shifted sampled or superstructure grating widely tunable twin-guide laser. *IEEE Photonics Technology Letters*, *13*(10), 1052-1054.

[46] Coldren, L. A. , Fish, G. A. , Akulova, Y. , et al. (2004). Tunable semiconductor lasers: A tutorial. *Journal of Lightwave Technology*, *22*(1), 193-202.

[47] Yamada, M. , Sakuda, K. (1987). Analysis of almost-periodic distributed feedback slab waveguides via a fundamental matrix approach. *Applied Optics*, *26*(16), 3474-3478.

[48] Schilereth, K. H. , Tacke, M. (1990) The complex propagation constant of multilayer waveguides: An algorithm for a personal computer. *IEEE Journal of Quantum Electronics*, *26*(4), 627-630.

[49] Wikipedia. (2009). Finite element method. *Wikipedia, The Free Encyclopedia*. Retrieved July 9, 2009, from http://en.wikipedia.org/w/index.php?title=Finite_element_method&oldid=301151970

[50] Wikipedia. (2009). COMSOL Multiphysics. *Wikipedia, The Free Encyclopedia*. Retrieved July 15, 2009, from http://en.wikipedia.org/w/index.php?title=COMSOL_Multiphysics&oldid=302179368

[51] Wikipedia. (2009). Finite-difference time-domain method. *Wikipedia, The Free Encyclopedia*. Retrieved June 2, 2009, from http://en.wikipedia.org/w/index.php?title=Finite-difference_time-domain_method&oldid=293985710

[52] Wikipedia. (2009). Maxwell's equations. *Wikipedia, The Free Encyclopedia*. Retrieved July 18, 2009, from http://en.wikipedia.org/w/index.php?title=Maxwell%27s_equations&oldid=302811822

[53] Yee, K. (1966). Numerical solution of initial boundary value problems involving Maxwell's equations in isotropic media *Antennas and Propagation, IEEE Transactions*, *14*, 302-307.

[54] Johnson, S. G. (2009). Meep. *Nanostructures and Computation Wiki at MIT*. Retrieved April 29, 2009, from http://ab-initio.mit.edu/wiki/index.php?title=Meep&oldid=3527

[55] Joannopoulos, J. D. , Johnson, S. G. , Meade, R. D. , and Winn, J. N. (2008). *Photonic Crystals: Molding the Flow of Light, second edition*. Princeton: Princeton Univ. Press.

[56] Wikipedia. (2009). Kerr effect. *Wikipedia, The Free Encyclopedia*. Retrieved July 3, 2009, from http://en.wikipedia.org/w/index.php?title=Kerr_effect&oldid=300107394

[57] Johnson, S. G. (2009). Materials in Meep. *Nanostructures and Computation Wiki at MIT*. Retrieved April 29, 2009, from http://ab-initio.mit.edu/wiki/index.php?title=Materials_in_Meep&oldid=3544